From Energy Deposition of Ionizing Radiation to Cell Damage Signaling: Benchmarking Simulations by Measured Yields of Initial DNA Damage after Ion Microbeam Irradiation

Geraldine Gonon, Carmen Villagrasa, Pascale Voisin, Sylvain Meylan, Marta Bueno Vizcarra, Mohamedamine Benadjaoud, Nicolas Tang, Frank Langner, Hans Rabus, Joan Francesc Barquinero, et al.

From Energy Deposition of Ionizing Radiation to Cell Damage Signaling: Benchmarking Simulations by Measured Yields of Initial DNA Damage after Ion Microbeam Irradiation

Géraldine Gonon[a*], Carmen Villagrasa[b], Pascale Voisin[a], Sylvain Meylan[b†], Marta Bueno[b], Mohamed Amine Benadjaoud[c], Nicolas Tang[b], Frank Langner[d], Hans Rabus[d], Joan-Francesc Barquinero[a‡], Ulrich Giesen[d], Gaëtan Gruel[a]

[*] Corresponding author email: geraldine.gonon@irsn.fr

Running title: From energy Deposition of Ionizing Radiation to Cell Damage Signaling

[a] Radiobiology of Accidental Exposure Laboratory, Direction of Human Health, Institut de Radioprotection et de Sûreté Nucléaire (IRSN), Fontenay-aux-roses, France
[b] Ionizing Radiation Dosimetry Laboratory, Direction of Human Health, Institut de Radioprotection et de Sûreté Nucléaire (IRSN), Fontenay-aux-roses, France
[c] Radiobiology and Regenerative Medicine Research Service, Direction of Human Health, Institut de Radioprotection et de Sûreté Nucléaire (IRSN), Fontenay-aux-roses, France
[d] Department 6.5 Radiation Effects, Physikalisch-Technische Bundesanstalt (PTB), Braunschweig, Germany
[†] Present address: Symalgo Technologies, Paris, France
[‡] Present address: Universitat Autònoma de Barcelona, Facultat de Biociències, Cerdanyola del Vallès, Spain

Abstract

Gonon, G., Villagrasa C. *et al.* From Energy Deposition of Ionizing Radiation to Cell Damage Signaling: Benchmarking Simulations by Measured Yields of Initial DNA Damage after Ion Microbeam Irradiation. *Radiat. Res.*

Advances in accelerator technology enabling radiotherapy performing conformal irradiations with charged hadronic species has brought benefits to patients but also, potentially, new risks. For a better understanding of the effects of ionizing radiation on tumor and surrounding tissue investigating and quantifying the relation between energy deposition at nanometric scale and the initial biological events is a key issue. Monte Carlo track structure simulation codes provide a powerful tool for investigating this relation; however, their success and reliability rely on their improvement and development accordingly to the dedicated biological data to which they are challenged. For this aim, microbeam facility that allows the controlling of the fluence down to one ion per cell nucleus was used to evaluate relative frequencies of DNA damage following the interaction between the incoming ion and DNA according to radiation quality. Primary human cells were exposed to α particles of three different energies with respective LETs of about 36, 85 or 170 $keV \cdot \mu m^{-1}$ at the cells' center position, or to protons (19 $keV \cdot \mu m^{-1}$). Statistical evaluation of nuclear foci formation (53BP1/γ-H2AX) observed by immunofluorescence and related to a particle traversal was undertaken in a large population of cell nuclei. The biological results were adjusted considering the factors that drive the experimental uncertainties and, then challenged with results using Geant4-DNA code modeling the ionizing particle interactions on a virtual phantom of the cell nucleus with the same mean geometry and DNA density as the cells used in our experiments. Both results show an increase of relative frequencies of foci (or simulated DNA damage) in cell nuclei as a function of increasing LET of the traversing particles, reaching a

quasi-plateau when the LET exceeds 80-90 keV·μm^{-1}. For the LET of an α particle ranging from 80-90 to 170 keV·μm^{-1}, 10-30% of the particle hits do not lead to DNA damage inducing 53BP1 or γ-H2AX foci formation.

Keywords: Microbeam, α particles, Protons, Radiobiology, High-LET, 53BP1, γ-H2AX, DNA damage, Track structure, Energy deposition, Geant-4 DNA, Monte Carlo simulation

Abbreviations

LET: linear energy transfer; RIF: radiation-induced foci; γ-H2AX: histone H2AX phosphorylated at serine 139; DAPI: 4', 6-diamino-2-phenylindole; SB: strand break; DSB(s): double-strand break(s); SD: standard deviation of a statistical distribution; SE: standard error; SEM: standard error of the sample mean; PBS: phosphate buffer saline; HEPES: 4-(2-hydroxyethyl)-1-piperazineethanesulfonic acid; BSA: bovine serum albumin; bp: base pair

Introduction

In radiation biology, the absorbed dose is used as a fundamental physical quantity on which we rely to estimate biological effects caused by ionizing radiation. Indeed, the absorbed dose is defined as the mean value of the specific energy, i.e. the ratio of the amount of energy deposited by ionizing radiation within a volume to the mass contained in that volume (unit: $J \cdot kg^{-1}$) (*1*). At *macroscopic* scale, such as tissues or organs, this mean value is a good estimate of the actual energy deposition in the volume. Nevertheless, even at the *macroscopic* scale equal absorbed doses of different types of radiation do not produce equal biological effects (*2, 3*). These differences are based on the distribution of imparted energy at the *microscopic* level (*2, 4*) which is not considered by the mean value given by the absorbed dose (*5, 6*). For microscopic volumes such as cells or subcellular structures, the distribution of the specific energy has a larger spread around the value of the absorbed dose, and this variability causes the differences between radiation qualities.

Charged particles lose their energy in a discontinuous manner, by inelastic collisions (mainly ionizations or excitations) with the target molecules. This leads to a spatially non-uniform distribution of the energy transfer points (the so-called track structure) which is concentrated along and around the path of a charged particle and depends on the ion type and energy. The linear energy transfer (LET) is the average energy deposited per traveled unit distance ($keV \cdot \mu m^{-1}$) (*7, 8*) and is often used as a *macroscopic* measure for the *microscopic* properties of radiation (*9*). It may be relevant at the cell or cell nucleus compartment levels (typically micrometers in size) but it does not account for random fluctuation in individual interactions of a given particle (*10*). Therefore, the *nanometric* resolution (scale of molecules

78 such as DNA molecules) of the individual energy depositions is required to better apprehend the
79 mechanisms of radiation effects at cellular or subcellular levels.
80 To overcome these limitations, Monte Carlo track structure simulation has become a powerful
81 tool to model energy deposition processes in biological structures such as cell nuclei. In some
82 cases, these codes can also handle the simulation of the physico-chemical and chemical processes
83 that follow in time the initial energy deposition and contribute to the final extent of DNA damage
84 for different radiation qualities (*11-13*). This simulation technique has a huge potential to better
85 explain the relation between energy deposition and the initial induced cellular damage. However,
86 the major difficulty is determining which descriptive parameters have the key role for a given
87 application (*9*). This simulation requires the estimation of some parameters (used either to
88 shortcut complex processes or as decision-criteria (*14*)) that are usually based on data coming
89 from biological experiments. Regarding the interaction, at the sub-micrometer level, between
90 charged hadronic species and living matter, the availability of relevant biological measurements
91 are rare or nonexistent. Designing and carrying out sets of suitable and dedicated biological
92 experiments, used as benchmarks so as to establish and adjust description parameters of the
93 phenomena at their origin, is essential for developing biophysical models as well as for
94 understanding the characteristics (physical or biological) of the initial radiation-induced damage
95 (*15*).
96 Recent advances in irradiation techniques and molecular biology have enabled the
97 observation and quantification of DNA damage of individual cells to single ionizing particles,
98 rather than averaging the effect over multiple cells and crossing ions. Indeed, microbeam
99 technology is offering the possibility to deliver a predetermined number of particles of a certain
100 radiation quality (type and energy) in a specific area of the cells, nucleus, or cytoplasm, with
101 micrometric spatial resolution (*16-18*). In parallel, the study of the initial induced cellular

damages related to a particle traversal performed on a large population of cells is achievable combining *in situ* observations on platforms of high-throughput microscopy including a powerful and robust infrastructure necessary for a massive image analysis.

Thus, the observation of nuclear foci formation by immunofluorescence, such as phosphorylation on serine 139 of the histone variant H2AX (γ-H2AX) and p53 binding protein-1 (53BP1), and the analysis of their characteristics (location, size, fluorescence intensity …) make a foci-based assay well suited to study markers of DNA damage produced by the ionizing particles. Phosphorylation of H2AX and relocation of 53BP1 are among the best characterized biomarkers for DNA DSB detection for which evidence suggests a close association between the two of them (*19-22*) although this point is still debated (*23-27*).

In this work, we investigate the relative frequencies of interaction between protons or α particles of different energies and DNA leading to at least one 53BP1 or γ-H2AX focus formation when the primary ionizing particles traverse the cell nucleus. We perform statistical evaluations of radiation-induced 53BP1 foci and γ-H2AX appearance in cell populations wherein each cell nucleus was traversed by a given number of particles delivered by the microbeam facility of Physikalisch-Technische Bundesanstalt (PTB) (*18*). The obtained foci number distributions were converted into relative frequencies of radiation-induced foci detected per particle track and corrected for the influence of the experiment's conditions. Indeed, all these factors should be considered to properly evaluate the relative frequencies of at least one 53BP1 or γ-H2AX focus formation as a function of the radiation LET. In parallel, simulation procedures using the Geant4-DNA Monte Carlo code were developed, to which the biological results are compared. This should allow the relation between the topology of energy deposition and early signaling of DNA damage to be elaborated.

Materials and methods

Cell culture

Cultures of primary human umbilical vein endothelial cells (HUVEC) were obtained from Lonza (Bâle; Suisse). All cells tested negative for mycoplasma, bacteria, yeast, and fungi. HIV-1, hepatitis B and hepatitis C were not detected for all donors. Cells at passage 2 (4–5 doubling population) were grown in endothelial cell growth media (EBM® and supplements) (Lonza) containing 4.72% (vol/vol) fetal bovine serum (Lonza), hydrocortisone, hFGF-B, VEGF, R3-IGF-1, ascorbic acid, hEGF, gentamicin and amphotericin-B (EGM-2BulletKit, Lonza). They were maintained at a temperature of 37°C in humidified incubators in an atmosphere of 5% CO_2 (vol/vol) in air. For experiments, cells were seeded at numbers that allowed them to reach the density-inhibited state within five days in 12.5 cm^2 polystyrene flasks. They were then fed twice on alternate days. The karyotype and the genomic stability of cells were evaluated to ensure an equivalent DNA content in all cells of a population (*28*).

Microbeam irradiation

The microbeam facility of Physikalisch-Technische Bundesanstalt (PTB) in Braunschweig, Germany, and the irradiation procedure have been previously described in detail (*18, 29, 30*). Briefly, protons and α particles were accelerated to the selected beam energies using an energy-variable cyclotron (The Cyclotron Corporation (TCC), model CV-28). Single-particle irradiation is facilitated with a signal from a detector system, consisting of thin scintillator and photo multiplier tube, which is used as a trigger for a fast beam deflector (*18*). The detection efficiency for ion passage and the spatial resolution have been estimated for each set of experiments. Owing

147 to energy losses of the particles in the microbeam exit window, a 10 or 40 µm-thick scintillator
148 and a 25 µm-thick bioFoil, the energy in the cell nuclei's center, obtained using SRIM code (*31*),
149 was 1.6 MeV for the protons and 17.8 MeV, 5.5 MeV, and 1.86 MeV for α particles. These
150 energy values correspond to average LET values of the ions of 19 $keV \cdot \mu m^{-1}$, 36 $keV \cdot \mu m^{-1}$,
151 85 $keV \cdot \mu m^{-1}$ and 170 $keV \cdot \mu m^{-1}$. The physical characteristics of the beam for the different
152 projectiles and energies used for biological experiments are reported in Table 1.

153 Spatial widths (full width at half maximum, FWHM) were achieved through focusing by the
154 electromagnetic elements of the microbeam. Before each setup of irradiation and using the same
155 type of dishes filled with medium, values in radial and axial (d1 x d2) directions at the level of
156 cells were noted and are listed in Table 1. The actual coordinates for a particular particle hit
157 follow a Gaussian distribution in x- ($\mu = 0$, $\sigma 1 = d1/2.355$) and y- ($\mu = 0$, $\sigma 2 = d2/2.355$) axes.
158 The detection threshold and noise events in the particle counter were also quantified or estimated
159 for each set of irradiations (Table 1). Indeed, a certain percentage of particles may be considered
160 as delivered by the microbeam due to the detection of noise events while none was emitted.
161 Conversely, an ionizing particle may be emitted but not detected due to the detection threshold,
162 leading to delivery of a second particle, with two particles delivered instead of one. This may
163 occur at each position of the pattern.

164 About 20 h before irradiations, confluent cell cultures were trypsinized and approximately
165 4,000 cells were seeded as a drop of 25–30 µL onto the 25 µm-thick replaceable hydrophilic
166 biofoils (polytetrafluoroethylene foil) (In Vitro Systems & Services, Göttingen, Germany) at the
167 base of specially designed stainless-steels dishes (*18*). The cell monolayer covers a circular area
168 with a diameter of about 4 mm. Dishes were maintained in 37°C humidified incubators in an
169 atmosphere of 5% CO_2 (vol/vol) in air for 2 h. Then, they were filled with medium and put back

in the incubators overnight. Cell nuclei were stained with 150 nM solution of Hoechst 33342 dye (17530, AAT Bioquest) for 30 min, rinsed with medium and then sealed with a cover glass. The cell dishes were positioned perpendicularly to the beam on a computer-controlled *xy*-stage (Märzhäuser, Wetzlar, Germany) mounted on an inverse microscope (Zeiss Axiovert 100). Then, they were scanned using a magnification x20 lens and a sensitive CCD camera (*18*), an LED-based light source Lumencor with 399 ± 9 nm wavelength for illumination and customized image analysis software to detect the location of each nucleus. The narrow bandwidths of the filters and light source allow a reduction of the possible interaction between UV light and Hoechst 33342 that leads to a background of γ H2AX foci formation. Special care was taken during all imaging and adjustment procedures to minimize the exposure times and to otherwise limit this effect. The dishes were maintained at 37°C during the scan and irradiation period, using a dish holder connected to a thermostat. Cell cultures were exposed to the particles and energies listed in Table 1. Each cell nucleus was targeted with the same pattern of five particles placed at the corners of a 4 µm side square with one target point in the middle, positioned at the barycenter of each cell nucleus (Fig. 1A). A typical duration for the whole procedure of the scan and irradiation of a cell dish containing 4,000 cells was about 30 minutes. After irradiation, the dishes with the cells were put back into the incubator. Control cell cultures (noted C) and sham-irradiated cell dishes (noted S) were handled in the same way as the test cultures, but were not irradiated. However, sham-irradiated cell cultures were subject to cell nuclei recognition.

In situ **immune detection of 53BP1 and γ-H2AX**

53BP1 and γ-H2AX are sensitive markers of DNA damages (*23, 32, 33*). Briefly, at different times after irradiation, cells were fixed with 4% paraformaldehyde and 2% sucrose in PBS for

15 min at room temperature, and rinsed with PBS. Subsequently, the cells were permeabilized with a Triton-X buffer [(0.5% TritonX-100, 300 mM sucrose, 3 mM $MgCl_2$, 20 mM HEPES Buffer (pH 7.4), 50 mM NaCl in water)] at 4°C for 3 min. The fixed and permeabilized cell monolayers were reacted with rabbit polyclonal anti-53BP1 (A300-272A, Bethyl) and mouse monoclonal anti-phospho-histone H2AX (Ser139) (05-636, Upstate) antibodies diluted respectively to 1:1000 (vol/vol) and 1:800 (vol/vol) in a blocking buffer [2% (vol/vol) BSA in PBS] for 1 h at room temperature which was followed by blocking buffer wash. After incubation for 1 h with goat anti-rabbit IgG coupled to Texas Red®-X (T6391, Invitrogen) and goat anti-mouse IgG_1 coupled to Alexa Fluor® 488 (A21121, Invitrogen) secondary antibodies, both diluted to 1:1000 in blocking buffer, the cells were washed in PBS. Nuclei were stained with 570 nM 4',6'-diamidino-2-phenylindol dihydrochloride (DAPI) solution (1050-A, Euromedex) for 5 min at room temperature. Prolong Gold antifade reagent (P36930, Invitrogen) was used in mounting the samples. Distributions of 53BP1 and γ-H2AX foci formation were examined.

Automated imaging acquisition

All the images within the same data set were captured with a Scan® platform (Olympus). It consists of an inverted microscope IX81 (Olympus) equipped with a motorized stage SCAN IM IX2 (Märzhäuser) and a MT20 fluorescence illumination system with fast filter wheel. The images were acquired using a UPLSAPO 100XO oil immersion objective lens (Olympus) (N.A. 1.4) associated with a high-resolution cooled digital CCD camera (ORCA-R2, Hamamatsu) and standard filter sets for DAPI ($\lambda_{ex}/\lambda_{em}$ = 342/450 nm), AlexaFluor488 ($\lambda_{ex}/\lambda_{em}$ = 488 nm/519 nm), and Texas Red-X ($\lambda_{ex}/\lambda_{em}$ = 595/615 nm). The image pixels were squares and their side length was measured to be 0.064 μm. The limit of resolution based on the N.A. of the objective lens in

the Alexa 488 channel is 0.2 μm (Rayleigh limit). Images were captured so that intensities for a given experiment were within the 12-bit linear range. In order to capture all nuclei in full, the images were acquired with an overlap of 15% between fields. For each channel, images were acquired as five z-stack images with step size of 0.25 μm between planes (one at the focal plane and four around). The images of the 3D stack were projected to 2D xy-images using maximum intensity projection.

Automated image analysis

The collected images were analyzed using the Olympus Scan® analysis software with edge segmentation algorithm that allows the simultaneous detection of nuclei (objects), 53BP1, and γ-H2AX foci (sub-objects) stained with different fluorescent probes. Nuclei and foci were identified using defining parameters such as intensity threshold for recognition, minimum and maximum object dimensions on a few example images and keeping the parameters constant for the entire set of images for a specific slide. Nuclei on the border were excluded from the analysis and duplicate nuclei due to overlap of 15% between images were suppressed. Automated image analysis enabled the efficient measurement of numerous topological parameters on foci and nuclei such as area, shape (i.e. circularity factor, elongation factor, etc.), integrated and mean intensity of DAPI, Alexa Fluor® 488 and Texas Red®-X, and relative positions in images and slides on the whole population of nuclei (~4,000 cells) exposed to the same irradiation condition. Data generated were plotted in two-dimensional dot plots and a first selection was made based on nucleus area and circularities which permits objects corresponding to clusters of nuclei and cellular debris to be removed from the analysis and for only isolated nuclei to be extracted (*28*). To eliminate complications in the interpretation of the results that arise from changes in

responses to ionizing radiation at different phases of the cell cycle (*34*), non-divided cells were selected. As the γ-H2AX foci background is higher in cell nuclei in divisions (S, G2, and metaphase) associated with DNA replication (*35*), non-replicating cells were discriminated from S-phase cells on the basis of integrated intensities of DAPI (DNA content) and Alexa Fluor® 488 (associated to γ-H2AX foci) of each object (*28*). Using this representation, a subpopulation of nuclei with low levels of integrated intensity of DAPI and Alexa Fluor® 488 can be sequentially separated not only in non-irradiated condition but also in irradiated condition (*28*). This allowed the selection of a well-defined population of nuclei mainly in G_0/G_1 phase of the cell cycle that correspond to approximately 1,500 to 3,000 cell nuclei per dish.

Simulation using Matlab

In this work, each cell nucleus of a population was targeted with the same pattern of irradiation. However, the real size of each nucleus together with microbeam characteristics such as beam size or detection thresholds and noise events in the particle counter could deviate from the square shape of the pattern and reduce the real number of particles reaching the particular nucleus. Following Hoechst staining, some cell nuclei were not detected and this ratio was estimated at 2% of the cell nuclei population by comparison of cell nuclei images as obtained during cell nuclei detection before irradiation and after DAPI staining. To estimate how features can affect the real number of hits and their localization in cell nuclei, calculations were undertaken using Matlab R2010b.

Morphology of cell nuclei

As the pattern is fixed, the morphology (size and orientation) of cell nuclei vary from one to the other and could have an impact on the number of particles hitting each cell nucleus in different replicate experiments. To adapt our script closer to reality, for each dish, each nucleus of the cell population was simulated as an ellipse considering their specific major and minor axes and their orientation (Supplementary Figures 1A and 2A-B) determined during image analysis and after fixation and staining with DAPI. Nuclear size varies with the equivalent major ellipse axis ranging between 13.7 and 23.8 µm and equivalent minor ellipse axis ranging between 9.2 and 16.0 µm whereas the nuclei area ranges between 103.2 and 277.6 µm² (Supplementary Fig. 3). The mean values ± SD were, respectively, (18.3 ± 1.4) µm, (12.2 ± 0.9) µm, and (175.9 ± 21.5) µm². The cell nuclei thickness was estimated using a confocal microscope on the same dishes used for the experiments as (2.4 ± 0.2) µm (SD).

Validation of the chosen irradiation pattern size

The beam parameters combined with the measured size and orientation of each cell nucleus and the size of the irradiation pattern allow a corrected number of ionizing particles reaching each cell nucleus to be assessed. Indeed, although the irradiation pattern is fixed, the coordinates of each particle hit of the irradiation pattern with respect to the nominal position had a Gaussian distribution along the x- ($\mu = 0$, $\sigma 1 = d1/2.355$) and y- ($\mu = 0$, $\sigma 2 = d2/2.355$) axes (Supplementary Fig. 1).

We attempted to minimize both the risk of missing a cell nucleus and the probability that two particles hit a given nucleus at less than 2 µm from each other. Indeed, two particle hits too close may lead to one big focus instead of two distinct foci. Supplementary Fig. 4, obtained by

simulation based on all size of cell nuclei analyzed during experiments, illustrates the relation between these phenomena for each dish studied (n=14). The likelihood of getting two particle hits at a distance of less than 2 µm from one another within a given nucleus (red curves) and the likelihood of cell nuclei being reached by less than five particle hits (blue curves) were calculated as a percentage for different side lengths of the square irradiation pattern taking into account the real size of each cell nuclei analyzed. The more the size of the pattern increases, the greater the probability that the ion misses the cell nucleus, and the lower the probability that two particles hit a nucleus with a distance of less than 2 µm from one another. Therefore, a value of 4 µm side of the irradiation pattern, as used in our experiments, is an optimum compromise that allows a maximum number of cells hit by exactly five particle trajectories to be obtained while limiting the probability of getting two particle hits within 2 µm of one another to around 20%. Despite the optimization of these two parameters, both have to be considered in order to calculate the probabilities of 53BP1 or γ-H2AX foci formation as a function of the LET of radiation.

Statistics

Part of the data was represented as relative frequency distributions of the number of 53BP1or γ-H2AX foci per nucleus (Fig. 2 and 4 and Supplementary Fig. 5). To take into account the inter-dish variability and to increase the statistical power of the analysis, data were pooled. The mean number of foci per nucleus (m) was calculated on pooled data and associated with the standard deviation (SD) computed as the square root of the variance of the given pooled distribution. A two-sample Kolmogorov-Smirnov test was performed to compare the distributions of the number of foci (γ-H2AX and 53BP1) per nucleus between control and sham-treated samples. It is a non-parametric test with no hypothesis on the form of the distribution (*36*).

306 The other part of the data was represented as relative frequencies of at least one focus
307 formation along a particle track traversal (Fig. 5). Considering raw data (Fig. 5A and B), the
308 means are the means of pooled data with the standard deviation associated. In Fig. 5C and D, the
309 means and bar errors represent the mean and the standard error obtained after a Monte Carlo
310 maximum likelihood optimization as proposed by Stram and Kopecky (*37*) in which the
311 parameter estimation and the corresponding inference is derived through Poisson likelihood
312 function integrated over the 525 corrected raw data simulations.

313

314 **Probabilities**

315 The relative frequencies of at least one radiation-induced focus formation per particle track
316 traversing the cell nucleus depend on the cell nucleus thickness. In the biological experiments,
317 the average cell nucleus thickness was 2.4 µm, whereas in the simulations a thickness of 2 µm
318 was considered. Therefore, it was necessary to derive a relation between the probabilities for the
319 formation of at least one observable focus along particle tracks of different lengths. Let's denote
320 by Δp the probability that a focus forms when the particle traverses a distance Δd and suppose
321 that Δp is independent of what happened before according to the Markov process referring to the
322 memoryless property of the process. Furthermore, the hypotheses were made that the DNA
323 density as well as the particle's LET are stationary along the particle track. Then, if n consecutive
324 path segments of length Δd forming a total path length of $n \times \Delta d$ are considered, for each of them
325 the probability of foci formation is equal to Δp and the number of segments in which foci
326 formation occurs would have a binomial probability distribution. The probability that in all of the
327 n path segments no foci is formed is then $(1-\Delta p)^n = (1-\Delta p)^{d/\Delta d}$. The expression $(1-\Delta p)^{d/\Delta d}$ can also
328 be used for the probability that there are no foci along a path length d if d is not an integer

multiple of Δd. The probability of detecting at least one focus when the particle travels a distance d is then $p_d = 1 - (1 - \Delta p)^{d/\Delta d}$, which can be solved to give $\Delta p = 1 - (1 - p_d)^{\frac{\Delta d}{d}}$. Thus, if two different path lengths d_1 and d_2 are considered, the conversion between the two probabilities is given by $p_{d_2} = 1 - \left(1 - p_{d_1}\right)^{\frac{d_2}{d_1}}$.

Monte Carlo simulation

A full simulation chain presented in detail in (*38*) was used in this work in order to simulate the DNA damage generated either by direct or indirect effects. In this simulation, three important aspects can be distinguished: the target description, the simulation of the physical interactions leading to direct DNA damage, and the chemical interactions leading to indirect DNA damage.

Target description

The target in the simulation consisted of a unique cell nucleus phantom representing the mean shape and dimensions of the endothelium cell nucleus irradiated in this work: a cylinder with an elliptical base of major semi-axis a = 9.5 μm, minor semi-axis b = 5.5 μm, and 2 μm height. These geometrical parameters were taken from a previous biological experimental measurement with endothelium cells grown in a different foil than the one used in the microbeam experiments. This phantom was then filled with the whole genome of a eukaryotic cell (~6 Gbp) that was built using the DNAFabric tool (*39*). This geometrical DNA description takes into account the complex organization of the chromatin at different scales as described in (*38*) and can be seen in Supplementary Fig. 7. Briefly, the ~6 Gbp of the genome were distributed in spherical regions representing chromatin domains containing ~1 Mbp that are placed homogeneously within the cell nucleus phantom in order to simulate cells in the G_0/G_1 phase of the cell cycle. Each of these

chromatin domains was filled with voxels containing a geometrical representation of the chromatin fiber of helicoidal shape. There are five different types of voxels that can be combined in order to form chromatin loops within the domains. The chromatin fiber itself is formed by nucleosomes placed helicoidally, each of them composed of a sphere representing the histone proteins and surrounded by two turns of the DNA double helix. Eventually, the DNA double helix is described at molecular scale, where each of the molecules of a nucleotide (sugar, phosphate, or base) is represented by a sphere whose volume is equal to the real molecular volume. In this target geometrical model, the nucleosomes in the chromatin fiber are linked forming a continuous DNA double helix for a given chromosome territory (group of chromatin domains).

Simulation of the physical stage

This target geometry built with DNAFabric software was then exported to the simulation chain, which uses a slightly modified version of Geant4-DNA (Geant4 V10.01) (*40, 41*) for simulating both the physical and chemical interactions after the passage of the protons or α particles through the cell nuclei.

In the Monte Carlo simulation of the physical stage, the default processes and models were used in this version of Geant4-DNA. These processes allow the transport of secondary electrons on liquid water down to a few eV (~7 eV) on an event-by-event basis and thus the track structure at nanometric scale of the ionizing radiation can be obtained. Nevertheless, they use physical models based on liquid water cross sections in order to calculate the type of interaction (elastic, ionization, and excitation) and the amount of energy that is deposited at each of the track interaction points. Thus, in this simulation, all the volumes in the target geometries were

considered to be composed of liquid water, the interaction cross sections of which are generally believed to be a good approximation for those of biological materials.

All the inelastic interactions leading to an energy deposition within the DNA volumes (sugar, phosphate, base, and hydration shell) were recorded to be analyzed afterwards and to calculate the number of direct damages as proposed in (*38*). Indeed, in this work, we considered that a direct strand break (SB_{dir}) was created if the amount of energy deposited by the physical interactions in the backbone region of one nucleotide (sugar + phosphate + hydration shell) exceeds 17.5 eV.

The simulation of the chemical stage

Physical interactions between the ionizing irradiation and the water molecules surrounding the DNA lead to water radiolysis and thus to the generation of water-derived radicals and solvated electrons that diffuse and react chemically between themselves but also with the DNA constituents. Some of these chemical reactions can then break the backbone and generate indirect strand breaks (SB_{ind}). In this work, the processes and models implemented in the Geant4-DNA V10.01 were used for simulating the water radiolysis and the radicals' diffusion and reactions. As explained in (*38*), new chemical reactions were included in the simulations in order to take into account the interactions between the radicals and the DNA constituents. Scavenging processes were taken into account by two methods. Firstly a specific reaction between histones (represented by a sphere of 2.4 nm radius) and all type of water radicals was included. In this reaction the water radical is absorbed and the histone remains unchanged, thus simulating the histone scavenging capacity. Nevertheless, in order to better simulate the whole contribution of scavengers pertaining to other radicals, other parameters are used in the calculation chain: chemical reactions are constrained in each voxel, i.e., chemical species cannot diffuse over the

voxel dimensions (50 nm length), and the chemical stage simulation is stopped 2.5 ns after the end of the physical stage. Finally, for the determination of indirect damage, it was considered that 40% of the reactions between the OH° radical and the phosphate molecules led to an induced strand break.

Clustering algorithm and statistical uncertainties

The locations in the DNA geometrical model of the direct and the indirect strand breaks were registered during the simulation for each track. The DBSCAN algorithm (*42*) was used in order to detect the damage clusters: a DSB damage cluster was defined when at least two SBs were located at a distance lower than 10 bp in the geometry and on opposite strands. Finally, the initial sets of clusters were also analyzed in order to determine whether they can be associated with each other and merged into a larger cluster. As a result of this simulation, we obtained a number of DSB clusters per track that can have different complexities, meaning a different number of SBs involved in the DSB clusters with a minimum of two SBs.

The simulations were performed using only one cell nucleus phantom traversed by 1 000 particles per energy. The required calculation time for the 1,000 tracks depends on the ionizing radiation LET, and for high LET values it could be as long as three weeks. The resulting statistical uncertainty (SEM) on the mean number of DSBs per 2 µm track is always lower than 5%. Finally, in order to calculate the number of foci that the DSBs could produce in the x-y plane, the hypothesis was done by considering that all individual DSBs along the track could lead to a focus. Therefore, if at least one DSB was formed along the track, whatever its z-coordinate is, the probability of observing a foci in the x-y plane was equal to 1. In figure 7, the three curves corresponding to the simulated results use this hypothesis but they change the complexity of the

DSBs that are taken into account in order to be considered as a potential focus (DSBs with at least two, three, or four SBs).

Results

Raw distribution of the number of 53BP1 and γ-H2AX foci in HUVEC cultures wherein each cell nucleus was targeted by 5 ions

Context

To study the interaction between a charged hadronic particle and DNA, we examined γ-H2AX and 53BP1 radiation-induced foci (RIF) formation *in situ* on a cell-by-cell basis and on a large number of human umbilical vein endothelial cells (HUVEC). As described previously (*28*), cells in G_0/G_1 were analyzed in order to eliminate potential interpretation issues due to the amount of DNA and/or interference from cellular responses to ionizing radiation at other phases of the cell cycle (*34*). Monolayers of primary HUVEC were irradiated perpendicularly with single ionizing particles at an ion microbeam that deposits energy along their track (Fig. 1A). Ionizing interactions in the cell nucleus lead to the formation of DNA double-strand breaks (DSBs) and the ensuing formation of foci (Fig. 1B). The number of produced foci depends on the radiation quality and the cell nuclei thickness which was estimated using confocal microscopy on the same dishes as used for the experiments and gave a mean thickness of 2.4 ± 0.2 µm (SD).

The radiation-induced 53BP1 or γ-H2AX foci in cells were detected *in situ* using a combination of a high-speed microscopy platform and automated image analysis. Images from multiple z-planes were acquired and then analyzed as collapsed maximum intensity projections

for improving the signal-to-noise ratio (*43*) when quantifying foci on the whole population of cell nuclei exposed to the same irradiation condition (Fig. 1C). The aim was to obtain the relative frequency of presence (or absence) of radiation-induced foci following one particle traversal within a typical endothelial cell nucleus of 2.4 µm mean thickness as a function of particle LET.

Characterization of 53BP1 and γ-H2AX foci background

Prior to irradiation, cell nuclei were stained with Hoechst-33342 dye and then scanned in order to be identified. This step may induce an increase in the 53BP1 and γ-H2AX signal that is independent of the irradiation. Therefore, additional cell samples that received no radiation were treated in parallel with irradiated dishes to evaluate 53BP1 and γ-H2AX foci background. Parts of them were sham-treated as they were subjected to cell nuclei recognition (using Hoechst-33342 staining), whereas other cell cultures were considered as controls.

In control and sham-treated samples, a significant number of cells also harbored foci, the frequencies of which slightly fluctuated between experiments. In Fig. 2, the data are represented as distributions of the number of 53BP1 or γ-H2AX foci per nucleus for the five and seven replicate experiments related, respectively, to control (Panel A) and sham-treated dishes (Panel B). For each background estimation experiment, between 427 and 3,793 cell nuclei in G_0/G_1 phase of the cell cycle were evaluated. To take into account the inter-dish variability, graphically viewable in Fig. 2A and 2B, and to increase the statistical power of the analysis, data were pooled. It reached a total of 8,132 and 15,236 cell nuclei for control and sham-irradiated samples, respectively. For both, 53BP1 or γ-H2AX, the distributions of the number of foci per nucleus are significantly different between control and sham-treated samples ($p<0.0001$). The mean number of 53BP1 foci per nucleus ± SD of control samples was 0.24 ± 0.67 while it reached 0.50 ± 0.86

462 for sham-treated samples (Fig. 2C). The percentage of cell nuclei without any 53BP1 focus
463 decreased from 83.5% for control to 65.4% for sham data while the percentage of cell nuclei with
464 at least one focus doubled going from 16.5% to 34.6%. Similarly, the mean number of γ-H2AX
465 foci per nucleus ± SD doubled from 0.09 ± 0.48 to 0.21 ± 0.72 between control and sham-treated
466 samples and the percentage of cell nuclei with at least one γ-H2AX focus increased from 5.1%
467 for control samples to 13.2% for sham-treated samples. Thus, the protocol of cell nuclei
468 recognition induces an increase of the number of cell nuclei harboring 53BP1 and γ-H2AX foci
469 in sham samples compared with control samples (Fig. 2C). It may be explained by the interaction
470 between Hoechst-33342 stain and photons in the 385–405 nm wavelength range exposure during
471 cell nuclei recognition, which has been reported to induce DNA damage (*44-46*). Consequently,
472 to obtain a number of radiation-induced 53BP1 or γ-H2AX foci per cell nucleus significantly
473 higher than the sham background, we performed experiments based on five particle traversals per
474 cell nucleus where the different ions were targeted at different positions in the cell nucleus.

475

476 **Distribution of the number of 53BP1 and γ-H2AX foci in HUVEC cell cultures wherein**
477 **each cell nucleus was targeted by five projectiles as a function of particle type and LET**

478 We examined 53BP1 and γ-H2AX foci *in situ*, in HUVEC cell cultures, fixed at 10 or
479 30 min after exposure to 1.86, 5.5, or 17.8 MeV α particles with respective LET values in the
480 center of the cell nuclei of about 170 $keV \cdot \mu m^{-1}$, 85 $keV \cdot \mu m^{-1}$, and 36 $keV \cdot \mu m^{-1}$ and also to
481 1.6 MeV protons (LET ~19 $keV \cdot \mu m^{-1}$). Each cell nucleus was targeted by five particles according
482 to a cross pattern with the four outer target points located on a square of 4 μm side length and the
483 middle one aimed at the barycenter of the cell nucleus (Fig. 3A). In Fig. 3B, 53BP1 (Panel B-2)
484 and γ-H2AX (Panel B-3) foci formation in a primary HUVEC cell nucleus (DAPI staining, Panel

B-1) after exposure to 17.8 MeV α particles reveals the irradiation pattern. The merged Fig. 3B (Panel B-4) shows a good superimposition of 53BP1 and γ H2AX foci. However, despite the theoretical five particle hits per nucleus, the number of foci observed per cell is not constant from one nucleus to another.

Distributions of the number of 53BP1 and γ-H2AX foci per nucleus were evaluated at 10 or 30 minutes after exposure to 1.6 MeV protons or 17.8 MeV, 5.5 MeV, or 1.86 MeV α particles (Fig. 4). 53BP1 foci distributions are similar for the two fixation times studied, either after irradiation to 1.6 MeV protons (LET ~19 keV·μm^{-1}) or 5.5 MeV α particles (LET ~85 keV·μm^{-1}) (Supplementary Fig. 5). Likewise, the results for DNA damage marker γ-H2AX follow the same propensity. As the two post-irradiation times tested (10 or 30 min) do not have any influence on the foci number distribution, only one time point for each condition of irradiation was considered in the further analysis. While theoretically five ionizing particles have reached each cell nucleus, the observed number of 53BP1 or γ-H2AX foci per nucleus can spread from 0 up to 10 and depends on the respective radiation quality used (Fig. 4).

Nonetheless, as previously indicated, our results showed a 53BP1 and γ-H2AX foci background (Fig. 2) that is not negligible and interferes, inevitably, with the observed results after exposure to ionizing particles. Moreover, the original irradiation pattern may have been distorted due to physical characteristics of the microbeam, such as detection system and beam size at the level of the cell culture, which, related to the size and orientation of cell nuclei, may lead to variation in the number of particle traversals per cell nucleus. It also has to be considered that two particle hits too close to each other may lead to one big focus instead of two distinct observable foci due to the limit of resolution based on the numerical aperture (N.A.) of the objective lens used in the microscope.

508 The measured distributions of number of detected foci were converted to relative
509 frequencies of radiation-induced 53BP1 or γ-H2AX foci per particle track as a function of the
510 radiation's LET taking into account all these factors biasing the experimental results.

511

512 **Evaluation of relative frequencies of at least one 53BP1 or γ-H2AX focus formation**
513 **following a particle traversal as a function of radiation's LET**

514 In order to evaluate relative frequencies of at least one interaction between an ionizing
515 particle and DNA along its track in nucleus thickness leading to 53BP1 or γ-H2AX foci
516 appearance, it is necessary to calculate, for each cell monolayer, the ratio by dividing the number
517 of appearing foci by the total number of particles emitted. However, corrections, applied on the
518 numerator and denominator of the ratio, allow us to apprehend the impact of different factors
519 mentioned above.

520 First of all, the relative frequencies of at least one focus formation per primary particle
521 track traversing 2.4 μm thickness of endothelial cell nucleus were determined based on raw data:

522 $$\frac{raw\ nb\ of\ foci}{5\ ionizing\ particles \times nb\ of\ cell\ nuclei} \qquad \text{(eq. 1)}$$

523 The relative frequencies of at least one focus formation per particle track based on raw
524 data are plotted in Fig. 5A and 5B as a function of the LET of protons (circles) and α particles
525 (diamonds) for each replicate experiment (open symbols) as well as the mean of all replications
526 for each irradiation condition (closed symbols) for, respectively, 53BP1 (Panel A) and γ-H2AX
527 (Panel B).

Secondly, as indicated above, for sham-treated samples subjected to cell nuclei recognition, around a third of cell nuclei present at least one 53BP1 focus whereas ~10% present at least one γ-H2AX focus (Fig. 2C). Thus, to remove foci background and consider only *radiation-induced foci*, we applied (eq. 2)

$$\frac{raw\ nb\ of\ foci - background\ nb\ of\ foci}{5\ ionizing\ particles \times nb\ of\ cell\ nuclei} \qquad \text{(eq. 2)}$$

where the background number of foci was generated by random sampling based on the distribution of pooled sham data.

Third, the interplay of physical characteristics of the microbeam, the cell's morphology, and the choice of the irradiation pattern, together with the detection threshold and noise events in the particle counter (as described in the materials and methods section), may affect the hit distribution per cell nucleus. To account for these factors, we simulated, for each nucleus of each replicate experiment, the microbeam irradiation sampling the ion-hit coordinates from the mentioned Gaussian distributions. Examples of graphic outputs of the sampling of hit patterns in different cell nuclei are shown in Supplementary Fig. 2. Although each cell nucleus theoretically should have received five particles according to the cross pattern, the number of traversing particles may vary slightly from one nucleus to another depending on the irradiation characteristics and cell nuclei geometry.

Table 2 reports in the fourth column the theoretical number of particles emitted from the microbeam (number of cell nuclei times five ionizing particles per nucleus) and in the fifth column the mean assessed number of particle hits in cell nuclei for each sample of each irradiation condition. On average, around 98% of the emitted particles hit their target (cell nuclei), and ~90% of the cell nuclei received five hits while the remaining cell nuclei (~10%)

were reached by mainly four or six particles. Therefore, the denominator of (eq. 2) was adjusted by an *estimated number of particle hits in the cell nuclei* such as in (eq. 3):

$$\frac{raw\ nb\ of\ foci - background\ nb\ of\ foci}{estimated\ nb\ of\ particle\ hits\ in\ the\ cell\ nuclei} \qquad \text{(eq. 3)}$$

The relative frequency estimators of at least one 53BP1 or γ-H2AX focus formation per particle track (± SE) based on raw data (purple symbols), taking into account sham background (green symbols) and combined with the accurate number of particles (orange symbols), were plotted in Fig. 5C and 5D. Although the general evolution of adjusted results versus LET is similar to estimators of the relative frequencies of at least one focus formation per particle track based on raw data (purple symbols), they follow a downward trend (green and orange markers). However, the corrections linked to real numbers of particles do not affect the results significantly (orange markers compared to green markers). The slight uncertainty in the number of ionizing particles reaching cell nuclei (Table 2) induces a slight increase in the estimation of relative frequencies (Fig. 5C and 5D).

Fourth, another correction factor taken into account in the analysis of the microbeam experiment results is the fact that two particle hits reaching a given cell nucleus at a distance less than 2 µm from each other may form *two* foci not distinguishable and analyzed as *one* focus formation. For a given size of the irradiation pattern, the occurrence of this phenomenon depends on the size of the particle beam, the number of particles that reach the cell nucleus, *and the relative frequencies of at least one focus formation per particle traversal itself* (that needs to be corrected). Therefore, using the simulated coordinates of each particle traversal calculated during the previous process of irradiation pattern reconstruction (as described in Supplementary Fig.1 and 2C), we simulated an artificial focus formation. This was performed by a Bernoulli schema

572 with success (conversion of a particle track into an artificial focus) probability increasing
573 iteratively from 0 to 1 by steps of 0.05. For a given probability of conversion, a set of artificial
574 foci was generated and pairs of foci located less than 2 μm apart from each other were combined
575 into one observable focus. Thus, we obtained a relation between relative frequencies of
576 supposedly observable foci and the underlying particles interacting at least once with DNA along
577 the particle track in the nucleus' thickness (Fig. 6). As this relation depends on the initial
578 irradiation characteristics (beam size and cell morphology), the relation was established for each
579 replicate experiment of each irradiation condition. Using those relations, we converted the
580 observed relative frequencies of at least one focus formation per particle traversal obtained by
581 (eq. 3) (orange curve in Fig. 5C and D) in the final estimate of relative frequencies of at least one
582 focus formation per particle traversal (red curve in Fig. 5C and D). Hence, the red curves of
583 Fig. 5C and D represent the most accurate estimates of relative frequencies of at least one
584 radiation-induced 53BP1 and γ-H2AX focus formation as a function of the particle LET when
585 traversing 2.4 μm thickness of an endothelial cell nucleus.

586 As the LET increases from about 19 $keV \cdot \mu m^{-1}$ for 1.6 MeV protons up to 36 $keV \cdot \mu m^{-1}$
587 and to 85 $keV \cdot \mu m^{-1}$ for, respectively, 17.8 and 5.5 MeV α particles, the estimated relative
588 frequency of at least one radiation-induced 53BP1 focus formation per particle track (± SE)
589 (Fig. 5C, red curve) increase progressively and significantly from 0.23 ± 0.03 up to 0.40 ± 0.01
590 and to 0.70 ± 0.02 53BP1 foci per particle hit. Beyond this value for the LET (85 $keV \cdot \mu m^{-1}$), the
591 relative frequency seems to reach a plateau with 0.66 ± 0.09 53BP1 foci per particle hit traversing
592 2.4 μm thickness of endothelial nucleus after exposure to 1.86 MeV α particles (170 $keV \cdot \mu m^{-1}$)
593 (Fig. 5C, red curve). Concerning γ-H2AX foci formation (Fig. 5D, red curve), although the
594 estimate of relative frequencies of at least one γ-H2AX focus formation per particle track (± SE)

follows the same increasing trend from 0.22 ± 0.04 for 1.6 MeV protons (19 keV·µm^{-1}) reaching 0.69 ± 0.04 for 1.86 MeV α particles (170 keV·µm^{-1}), the slope is less pronounced. Besides, concerning γ-H2AX foci formation, the values are not significantly different between 1.6 MeV protons (19 keV·µm^{-1}) and 17.8 MeV α particles (36 keV·µm^{-1}).

Considering α particle exposure, convergence of relative frequencies of at least one 53BP1 focus formation per particle track after exposure to 5.5 and 1.86 MeV α particles with respective LETs in the nucleus of 85 and 170 keV·µm^{-1} is noticeable. This suggests that, for the same type of particle with high LETs (85 and 170 keV·µm^{-1}), the probability that an interaction occurs between particle and DNA leading to detectable DNA damage (53BP1 or γ-H2AX focus formation) is similar and is evaluated as ~0.65. As a result, in 35% of cases, high LET α particles do not induce DNA damage leading to 53BP1 foci formation.

As explained in the introduction, these biological data were compared with results obtained by Monte Carlo simulations, modeling the ionizing particle interactions on a virtual phantom of the 2 µm-thick cell nucleus filled with a DNA geometrical model in the G_0/G_1 phase. However, subsequently, the cell nuclei thickness was estimated using a confocal microscope on the same dishes used for the experiments as (2.4 ± 0.2) µm (SD). Accordingly, for the sake of comparison to the simulations, the biological relative frequencies of at least one focus formation following a particle traversal were, beforehand, converted to the probability per 2 µm path length using a relation based on Markov property with the quantity of DNA traversed and LETs of the particle constant as explained in the materials and methods section. As Fig. 7 shows (light and dark grey for, respectively, 53BP1 and γ-H2AX foci formation), in doing so, all the frequency values were reduced. However, the trend of the curves of converted data as a function of the LET of the primary particle is similar to those of the experimental results.

618

619 ***In silico* estimate of probability of at least one radiation-induced focus formation per**
620 **particle track traversing the endothelial cell nucleus and comparison with biological results**

621 Simulation of particle interactions with DNA

622 The individual energy depositions originated from the projectile (proton or α particle) or
623 the secondary electrons were simulated using the Monte Carlo code Geant4-DNA. This
624 simulation allows the calculation of the physical and chemical interactions that can damage the
625 DNA target (direct and indirect effects, respectively). In particular, we simulated DNA DSB
626 clusters that are related to foci appearance. These are generated by the interaction between initial
627 energy depositions caused by ionizing radiation and the cell target as explained in the materials
628 and methods section and in (*38*). From the estimated values of DSB clusters produced along
629 particle tracks traversing the cell nucleus, a 2D projection allowed simulated foci to be obtained
630 that can be related to what is observable with microscopy methodology used in biological
631 experiments (Fig. 1). It is worth noting that, in this work, the hypothesis was made that each
632 simulated DSB cluster along the track is converted into a detectable focus. Nevertheless, and as
633 explained in the materials and methods section, the definition of the cluster damage that could
634 lead to a focus was studied and changed from all DSB clusters (at least two strand breaks with
635 one in an opposite strand to the others) to more complex DSB clusters (at least three or four
636 strands breaks contained in the clustered damage).

637 From this consideration, relative frequencies based on Monte Carlo simulation of at least one
638 focus formation were estimated for 0.5, 1, 10, or 20 MeV protons or 1.66, 5.27, or 17.39 MeV
639 α particles and plotted (blue, green and red lines) as a function of the LET of the primary protons

640 (circles) or α particles (diamonds) (Fig. 7). The choice of the α particle's energy in the simulation
641 was chosen to approach the estimated LET of the α particles at the cell center position in the
642 microbeam experiment. The additional protons' energies were also interesting to appreciate the
643 evolution of the simulation at lower LET.

644 Comparable to corrected biological data (light and dark grey for 53BP1 and γ-H2AX foci
645 formation, respectively), the simulated relative frequencies of at least one radiation-induced focus
646 formation per particle track (Fig. 7, blue, green and red lines) increase gradually. Considering
647 DSB clusters induced by at least two breaks in opposite strands (Fig. 7, blue line), the values rise
648 from 0.058 (corresponding to LET ~2.7 keV·μm^{-1} for 20 MeV protons) up to 0.9 foci per particle
649 track (corresponding to LET ~83 keV·μm^{-1} for 5.27 MeV α particles). At about a LET value of
650 ~80 keV·μm^{-1}, the curve seems to reach a plateau with simulated relative frequencies of ~0.9 foci
651 per particle hit traversing. Although the simulated relative frequencies follow the same tendency
652 of the corrected biological data (grey curves), this simulation (blue line) overestimates the
653 relative frequencies of experimental foci, whereas the simulation taking into consideration at least
654 four strand breaks to induce a DSB cluster underestimates the relative frequency except for the
655 last point (5.27 MeV α particles, LET ~83 keV·μm^{-1}). Moreover, the quasi-plateau found in the
656 simulated data (blue line) corresponds to a probability of at least one focus formation within a
657 track hitting the cell nucleus of ~1 within the statistical uncertainty and not to a saturation of the
658 DNA damage value. Indeed, the mean number of simulated DSB clusters along the track
659 increases with the LET of the incident particle going from 6.6 to 18.3 for, respectively, 5.27 MeV
660 (LET ~83 keV·μm^{-1}) and 1.66 MeV (LET ~193 keV·μm^{-1}) α particles. Therefore, we can
661 conclude that the probability of having at least one focus along a 2 μm track traversing the cell

nucleus is already ~1 for α particles of 5.27 MeV (LET ~83 keV·μm^{-1}) and thus, still 1 for 1.66 MeV α particles (LET ~193 keV·μm^{-1}).

Discussion

Computational modeling allows the simulation and the study of the behavior of complex systems containing numerous variables that characterize the system being studied. As with all computational models, multi-scale approaches of energy deposition of ionizing particles must be rigorously tested against relevant biological data for proper validation prior to use as experimental constructs (*47*). Indeed, the multi-scale code developed and applied here should give information on how energy is deposited along the track of an ionizing particle and allow the biological effects to be predicted. The relation between the topology of energy deposition and the initial biological events (mainly DNA damage) is the first step in this process. Here, we provide sets of dedicated biological experiments that are compared to results of track structure Monte Carlo simulations using the Geant4-DNA multiparticle transport code.

When DNA is exposed to DNA-damaging agents, a plethora of damage-sensing and repair proteins localize at the site of DNA damage. Here, we used the formation of 53BP1 and γ-H2AX foci as a biomarker of DNA double-strands breaks (*24, 48*) to investigate radiation-induced damage per particle track in primary human endothelial cell (HUVEC) cultures after exposure to 1.6 MeV protons or to 1.86, 5.5, or 17.8 MeV α particles using the microbeam facility at the PTB. Due to the orthogonal configuration of the irradiation, 53BP1 and γ-H2AX foci observed in irradiated cell culture were expected to represent one ionizing particle traversal.

682 To estimate accurately the relative frequencies of at least one focus formation related to a
683 particle traversal, large numbers of cell nuclei were analyzed, and results were represented as a
684 function of the particle LET.

685 Beforehand, it is interesting to highlight the variabilities in control and in sham-treated
686 samples, namely in the number of cells that harbored 53BP1 or γ-H2AX foci which slightly
687 fluctuated between experiments (Fig. 2). First of all, the number of 53BP1 foci per nucleus is
688 higher than the number of γ-H2AX foci per nucleus, both in control and in sham-treated samples.
689 Indeed, it appeared that 53BP1 foci recognition in both control and sham-treated samples was
690 impeded due to basal pan nuclear distribution with some large nuclear "dots", whereas post-
691 irradiation analysis is more reliable due to protein relocation to the site of DNA damage (*49*).
692 Conversely, as the selection of cell nuclei in G_0/G_1 phase of cell cycle was based on integrated
693 intensities of DAPI and Alexa Fluor® 488 (*28*), it may have induced a more stringent
694 discrimination based on γ-H2AX, hence a more robust measure of γ-H2AX foci in control and
695 sham samples compared to the 53BP1 foci measure. However, although the γ-H2AX foci
696 background is lower, the speckled nuclear patterns do not disappear post-irradiation; thus
697 radiation-induced γ-H2AX foci detection is less accurate. Moreover, the increased number of cell
698 nuclei with 53BP1 and γ-H2AX foci in sham samples compared to control samples (Fig. 2C)
699 confirms that pretreatment with Hoechst-33342 enhanced mainly the UV-induced (385–405 nm)
700 γ-H2AX foci formation (*44-46*). Consequently, in both cases, it is required to take into
701 consideration respective sham-induced foci in the post-irradiation analysis. However, for the
702 analysis of radiation-induced 53BP1 foci, the "cleaning" based on 53BP1 expression in sham-
703 treated samples may have induced the removal of non-specific 53BP1 foci. There is no perfect
704 biomarker, but it is necessary to know the pros and cons of each of them. Therefore, the intrinsic
705 difference between the two biomarker curves should not be interpreted as any difference between

53BP1 or γ-H2AX foci formation following ionizing exposure in our experiment (Fig. 5). In this study, we focus on the trend of the relative frequencies of DNA DSBs, induced by ionizing particles with different LET values traversing 2.4 μm thickness of endothelial cell nucleus.

Even though the impact of background foci corrections based on sham data is important (Fig. 5, purple to green curve), the uncertainties associated with corrections are small compared to variabilities between replicate experiments on the raw data. The same applies to the uncertainties of adjustments related to physical microbeam characteristics as well as to the correction based on the size and distance between foci.

Once all corrections are considered (Fig. 5C and D, red curves), for none of the radiation qualities tested do the relative frequencies of at least one 53BP1 or γ-H2AX focus formation per particle track traversal reach 1. In both cases, the relative frequencies increase with the LET up to 85 $keV \cdot \mu m^{-1}$ (5.5 MeV α particles) where a quasi-plateau is observed. At this LET value, ~30–40% of particle hits do not induce DNA damage detected by a 53BP1 or a γ-H2AX focus. In this case, either the primary ionizing particle does not hit any DNA on the 2.4 μm-thick nucleus traversed, or the induced DNA damages does not lead to a 53BP1 or γ-H2AX signal observable 10 or 30 minutes post-irradiation or, possibly, with a different kinetic. Considering the first assumption, if the DNA was occupying the cell nucleus evenly (about 2.2% in volume for the endothelial cell nucleus used in our experiments), the generation of DNA damage following ionizing particle traversal would be a certain event. The relative frequencies of at least one 53BP1 and γ-H2AX focus per particle track would then be 1. The probability of DNA damage is linked primarily to track structure (i.e. ionization density and core size) in relation to target density (i.e. chromatin structure) (*50-53*).

728 The trend of relative frequencies of at least one focus formation per particle track
729 traversing a certain thickness of endothelial nucleus is confirmed by the simulation (Fig. 7). From
730 the estimated values of DNA DSBs produced along the particle tracks, a 2D projection allowed a
731 number of simulated foci to be obtained that can be related to what is observable with
732 microscopy.

733 The quasi-plateau observable *in vitro* is also observable *in silico* above a LET of
734 ~80 keV·μm^{-1}. However, as indicated in the results section, this quasi-plateau represents a
735 probability of ~1 within the statistical uncertainty as demonstrated by the mean number of
736 simulated DSBs per track that continue to increase between LETs of ~83 and ~193 keV·μm^{-1}
737 (6.576 and 18.342 respectively) (Supplementary Table 1). This result is intimately linked to the
738 hypothesis used in the simulation that every calculated DNA DSB leads to a visible focus
739 independent of its complexity or location in the DNA structure. Therefore, we decided to take
740 into consideration this complexity and test if this could be an indicator of foci formation. To do
741 so, we evaluated the probability of foci formation depending on the number of DNA strand
742 breaks (SBs) contained in the clustered damage and we increased from the minimum of two DNA
743 SBs used in the results to clustered DNA damage with a minimum of three or four DNA SBs
744 required to induce DNA DSB (Supplementary Table 1). As it can be seen in Fig. 7, the absolute
745 values on the calculated probability of foci formation are quite close to the experimental data for
746 clusters with a minimum of three SBs. Nevertheless, no saturation is observed for probabilities
747 between LET values of ~83 and ~193 keV·μm^{-1}, which indicates that, despite a decrease in the
748 absolute values compared to the initially simulated results, the increase in the number of
749 simulated foci with LET does not follow the biological observations and thus DSB complexity
750 itself cannot be the explanation of this observed quasi-plateau at probabilities around 0.7.

In the current state of this simulation, as in other models (*54*), a homogeneous distribution of DNA inside the nucleus is assumed and a unique chromatin structure (close to heterochromatin) is considered. In reality, local DNA concentration and compaction may vary in the nucleus. Differences in DNA density between euchromatin and heterochromatin likely influence the probability of inducing DNA damage but also the accessibility of DNA lesions and the speed of their processing (*55*). In addition, the chromatin remodeling process must not be forgotten, as it may play an essential role in orchestrating the recruitment of repair proteins and their access to the damaged regions of the DNA (*56-58*). Taking into account DNA density and compaction is in development and is expected to influence the simulation results. The possibility that 53BP1 and γ-H2AX foci formation may give a signal only for a subsection of DNA DSB damage or that it does it with a different kinetic and leads to underestimation from the present biological data cannot be excluded either.

The data reported here highlight that biological data such as the frequency of DNA DSB damage induced along an ionizing particle track may not only be a function of the macroscopic parameter LET. The results show an initial increase of at least one focus formation along the track as the LET increases until saturation occurs at a LET around 85 $keV \cdot \mu m^{-1}$. Additional experiments are necessary to complete the current curve with ions with intermediate LETs or with LETs higher than those analyzed and by using biomarkers known to be more specific to other types of DNA damage (DNA single strand break, base damage, sugar damage etc.). Other configurations of irradiation which provide access to the number of foci formed along the track (*50, 51, 59-61*) and not only in 2D projection associated to binary response (presence or absence) would be of interest to nourish the simulation.

Based on the same analysis, studying the early biological effects of two types of ions with the same LET would be of great interest to study the effects of their specific track diameter and

ionization density. In this context, the improvement of DNA density description *in silico* that varies as a function of cell types and phase of cell cycle needs to be developed in order to be implemented in the simulation. The combination of biological experiments and simulation developments allow the nature of biological effects induced by radiation to be deciphered along with all reactions around the primary ionizing events. It is highly informative towards understanding the spectrum of biological effects induced after exposure to single high-LET particles. Together, these studies may greatly contribute to our understanding of the link between energy deposition along the track and the initial DNA damage induced.

Acknoledegments

We thank O. Döhr, H. Eggestein, T. Heldt and M. Hoffmann for the operation of the PTB ion accelerators, and A. Heiske, T. Klages and J. Rahm for their support with the irradiation of cells.

This work was carried out within the European Metrology Research Programme (EMRP) Joint Research Project SIB06 "Biologically Weighted Quantities in RadioTherapy" (BioQuaRT). The EMRP was jointly funded by the EMRP participating countries within EURAMET and the European Union.

References

1. ICRU Report 85. Journal of the International Commission on Radiation Units and Measurements. 2011;11(1):1-31.

795 2. Hall EJ, Giaccia AJ. Radiobiology for the radiologist. 7th ed. Philadelphia: Wolters
796 Kluwer Health/Lippincott Williams & Wilkins; 2012.
797 3. Barendsen GW, Walter HMD. Effects of Different Ionizing Radiations on Human Cells in
798 Tissue Culture: IV. Modification of Radiation Damage. Radiat Res. 1964;21(2):314-29.
799 4. Cember H. Introduction to health physics. 3rd ed. New York: McGraw-Hill, Health
800 Professions Division; 1996.
801 5. Nettelbeck H, Rabus H. Nanodosimetry: The missing link between radiobiology and
802 radiation physics? Radiation Measurements. 2011;46(9):893-7.
803 6. Palmans H, Rabus H, Belchior AL, Bug MU, Galer S, Giesen U, et al. Future
804 development of biologically relevant dosimetry. The British Journal of Radiology.
805 2015;88(1045):20140392.
806 7. Zirkle RE, Marchbank DF, Kuck KD. Exponential and sigmoid survival curves resulting
807 from alpha and x irradiation of Aspergillus spores. J Cell Physiol Suppl. 1952;39(Suppl. 1):78-
808 85. Epub 1952/03/01.
809 8. ICRU Reports 16. Journal of the International Commission on Radiation Units and
810 Measurements. 1970;os9(1):48-9.
811 9. Goodhead DT. Relationship of Microdosimetric Techniques to Applications in Biological
812 Systems. In: Kase KR, Bjärngard BE, Attix FH, editors. The Dosimetry of Ionizing Radiation.
813 New York: Academic Press; 1987. p. 1-89.
814 10. Kellerer AM, Chmelevsky D. Concepts of microdosimetry. III. Mean values of the
815 microdosimetric distributions. Radiat Environ Biophys. 1975;12(4):321-35. Epub 1975/12/04.
816 11. Friedland W, Paretzke HG, Ballarini F, Ottolenghi A, Kreth G, Cremer C. First steps
817 towards systems radiation biology studies concerned with DNA and chromosome structure within
818 living cells. Radiat Environ Biophys. 2008;47(1):49-61. Epub 2008/01/15.

12. Nikjoo H, Uehara S, Wilson WE, Hoshi M, Goodhead DT. Track structure in radiation biology: theory and applications. Int J Radiat Biol. 1998;73(4):355-64. Epub 1998/05/20.

13. Nikjoo H, Uehara S, Emfietzoglou D, Cucinotta FA. Track-structure codes in radiation research. Radiation Measurements. 2006;41(9–10):1052-74.

14. Villagrasa C, Meylan S, Gonon G, Gruel G, Giesen U, Bueno M, et al., editors. Geant4-DNA simulation of DNA damage caused by direct and indirect radiation effects and comparison with biological data. Proceedings of the 13th International Conference on Radiation Shielding and 19th Topical Meeting of the Radiation Protection and Shielding Division of the American Nuclear Society-2016; 2017; Paris, France: EPJ Web of Conferences.

15. Rabus H, Palmans H, Hilgers G, Sharpe P, Pinto M, Villagrasa C, et al., editors. Biologically weighted quantities in radiotherapy: An EMRP joint research project. 16th International Congress of Metrology; 2014; Paris: EDP Sciences.

16. Hei TK, Wu LJ, Liu SX, Vannais D, Waldren CA, Randers-Pehrson G. Mutagenic effects of a single and an exact number of alpha particles in mammalian cells. Proc Natl Acad Sci U S A. 1997;94(8):3765-70. Epub 1997/04/15.

17. Wu LJ, Randers-Pehrson G, Xu A, Waldren CA, Geard CR, Yu Z, et al. Targeted cytoplasmic irradiation with alpha particles induces mutations in mammalian cells. Proc Natl Acad Sci U S A. 1999;96(9):4959-64. Epub 1999/04/29.

18. Greif K-D, Brede HJ, Frankenberg D, Giesen U. The PTB single ion microbeam for irradiation of living cells. Nuclear Instruments and Methods in Physics Research Section B: Beam Interactions with Materials and Atoms. 2004;217(3):505-12.

19. Rothkamm K, Lobrich M. Evidence for a lack of DNA double-strand break repair in human cells exposed to very low x-ray doses. Proc Natl Acad Sci U S A. 2003;100(9):5057-62. Epub 2003/04/08.

20. Kuhne M, Riballo E, Rief N, Rothkamm K, Jeggo PA, Lobrich M. A double-strand break repair defect in ATM-deficient cells contributes to radiosensitivity. Cancer Res. 2004;64(2):500-8. Epub 2004/01/28.

21. Lobrich M, Rief N, Kuhne M, Heckmann M, Fleckenstein J, Rube C, et al. In vivo formation and repair of DNA double-strand breaks after computed tomography examinations. Proc Natl Acad Sci U S A. 2005;102(25):8984-9. Epub 2005/06/16.

22. Mariotti LG, Pirovano G, Savage KI, Ghita M, Ottolenghi A, Prise KM, et al. Use of the gamma-H2AX assay to investigate DNA repair dynamics following multiple radiation exposures. PLoS One. 2013;8(11):e79541. Epub 2013/12/07.

23. Rogakou EP, Pilch DR, Orr AH, Ivanova VS, Bonner WM. DNA double-stranded breaks induce histone H2AX phosphorylation on serine 139. J Biol Chem. 1998;273(10):5858-68. Epub 1998/04/16.

24. Kinner A, Wu W, Staudt C, Iliakis G. Gamma-H2AX in recognition and signaling of DNA double-strand breaks in the context of chromatin. Nucleic Acids Res. 2008;36(17):5678-94. Epub 2008/09/06.

25. Goodarzi AA, Jeggo P, Lobrich M. The influence of heterochromatin on DNA double strand break repair: Getting the strong, silent type to relax. DNA Repair. 2010;9(12):1273-82.

26. Costes SV, Chiolo I, Pluth JM, Barcellos-Hoff MH, Jakob B. Spatiotemporal characterization of ionizing radiation induced DNA damage foci and their relation to chromatin organization. Mutat Res. 2010;704(1-3):78-87. Epub 2010/01/12.

27. Nikitaki Z, Nikolov V, Mavragani IV, Plante I, Emfietzoglou D, Iliakis G, et al. Non-DSB clustered DNA lesions. Does theory colocalize with the experiment? Radiation Physics and Chemistry. 2016;128:26-35.

866 28. Gruel G, Villagrasa C, Voisin P, Clairand I, Benderitter M, Bottollier-Depois JF, et al.
867 Cell to Cell Variability of Radiation-Induced Foci: Relation between Observed Damage and
868 Energy Deposition. PLoS One. 2016;11(1):e0145786. Epub 2016/01/05.
869 29. Brede HJ, Greif KD, Hecker O, Heeg P, Heese J, Jones DT, et al. Absorbed dose to water
870 determination with ionization chamber dosimetry and calorimetry in restricted neutron, photon,
871 proton and heavy-ion radiation fields. Phys Med Biol. 2006;51(15):3667-82. Epub 2006/07/25.
872 30. Mosconi M, Giesen U, Langner F, Mielke C, Dalla Rosa I, Dirks WG. 53BP1 and MDC1
873 foci formation in HT-1080 cells for low- and high-LET microbeam irradiations. Radiat Environ
874 Biophys. 2011;50(3):345-52.
875 31. Ziegler JF. Computer code SRIM-2013.00 - Particle interaction with matter, SRIM
876 (Stopping and Range of Ions in Matter) Available from: http://www.srim.org/.
877 32. Rappold I, Iwabuchi K, Date T, Chen J. Tumor suppressor p53 binding protein 1 (53BP1)
878 is involved in DNA damage-signaling pathways. J Cell Biol. 2001;153(3):613-20. Epub
879 2001/05/02.
880 33. Schultz LB, Chehab NH, Malikzay A, Halazonetis TD. p53 binding protein 1 (53BP1) is
881 an early participant in the cellular response to DNA double-strand breaks. J Cell Biol.
882 2000;151(7):1381-90. Epub 2001/01/03.
883 34. Terasima T, Tolmach LJ. Changes in x-ray sensitivity of HeLa cells during the division
884 cycle. Nature. 1961;190:1210-11. Epub 1961/06/24.
885 35. MacPhail SH, Banath JP, Yu Y, Chu E, Olive PL. Cell cycle-dependent expression of
886 phosphorylated histone H2AX: reduced expression in unirradiated but not X-irradiated G1-phase
887 cells. Radiat Res. 2003;159(6):759-67. Epub 2003/05/20.
888 36. Massey FJ. The Kolmogorov-Smirnov Test for Goodness of Fit AU. Journal of the
889 American Statistical Association. 1951;46(253):68-78.

37. Stram DO, Kopecky KJ. Power and uncertainty analysis of epidemiological studies of radiation-related disease risk in which dose estimates are based on a complex dosimetry system: some observations. Radiat Res. 2003;160(4):408-17. Epub 2003/09/13.

38. Meylan S, Incerti S, Karamitros M, Tang N, Bueno M, Clairand I, et al. Simulation of early DNA damage after the irradiation of a fibroblast cell nucleus using Geant4-DNA. Scientific reports. 2017;7(1):11923. Epub 2017/09/22.

39. Meylan S, Vimont U, Incerti S, Clairand I, Villagrasa C. Geant4-DNA simulations using complex DNA geometries generated by the DnaFabric tool. Computer Physics Communications. 2016;204:159-69.

40. Incerti S, Baldacchino G, Bernal M, Capra R, Champion C, Francis Z, et al. THE GEANT4-DNA PROJECT. International Journal of Modeling, Simulation, and Scientific Computing. 2010;01(02):157-78.

41. Bernal MA, Bordage MC, Brown JMC, Davidkova M, Delage E, El Bitar Z, et al. Track structure modeling in liquid water: A review of the Geant4-DNA very low energy extension of the Geant4 Monte Carlo simulation toolkit. Phys Med. 2015;31(8):861-74. Epub 2015/12/15.

42. Ester M, Kriegel H-P, Sander J, Xu X. A density-based algorithm for discovering clusters a density-based algorithm for discovering clusters in large spatial databases with noise. Proceedings of the Second International Conference on Knowledge Discovery and Data Mining; Portland, Oregon. 3001507: AAAI Press; 1996. p. 226-31.

43. McVean A, Kent S, Bakanov A, Hobbs T, Anderson R. Development and validation of 'AutoRIF': software for the automated analysis of radiation-induced foci. Genome integrity. 2012;3(1):1. Epub 2012/01/28.

44. Limoli CL, Ward JF. A new method for introducing double-strand breaks into cellular DNA. Radiat Res. 1993;134(2):160-9. Epub 1993/05/01.

914 45. Khalil A, Morgan RN, Adams BR, Golding SE, Dever SM, Rosenberg E, et al. ATM-
915 dependent ERK signaling via AKT in response to DNA double-strand breaks. Cell Cycle.
916 2011;10(3):481-91. Epub 2011/01/26.
917 46. Singh S, Dwarakanath BS, Mathew TL. DNA ligand Hoechst-33342 enhances UV
918 induced cytotoxicity in human glioma cell lines. Journal of Photochemistry and Photobiology B:
919 Biology. 2004;77(1–3):45-54.
920 47. Walpole J, Papin JA, Peirce SM. Multiscale computational models of complex biological
921 systems. Annual review of biomedical engineering. 2013;15:137-54. Epub 2013/05/07.
922 48. Groesser T, Chang H, Fontenay G, Chen J, Costes SV, Helen Barcellos-Hoff M, et al.
923 Persistence of gamma-H2AX and 53BP1 foci in proliferating and non-proliferating human
924 mammary epithelial cells after exposure to gamma-rays or iron ions. Int J Radiat Biol.
925 2011;87(7):696-710. Epub 2011/01/29.
926 49. Anderson L, Henderson C, Adachi Y. Phosphorylation and rapid relocalization of 53BP1
927 to nuclear foci upon DNA damage. Mol Cell Biol. 2001;21(5):1719-29. Epub 2001/03/10.
928 50. Costes SV, Ponomarev A, Chen JL, Nguyen D, Cucinotta FA, Barcellos-Hoff MH.
929 Image-based modeling reveals dynamic redistribution of DNA damage into nuclear sub-domains.
930 PLoS computational biology. 2007;3(8):e155. Epub 2007/08/07.
931 51. Ponomarev AL, Cucinotta FA. Novel image processing interface to relate DSB spatial
932 distribution from experiments with phosphorylation foci to the state-of-the-art models of DNA
933 breakage. Radiation Measurements. 2006;41(9):1075-9.
934 52. Cucinotta FA, Pluth JM, Anderson JA, Harper JV, O'Neill P. Biochemical Kinetics Model
935 of DSB Repair and Induction of γ-H2AX Foci by Non-homologous End Joining. Radiat Res.
936 2008;169(2):214-22.

937 53. Ponomarev AL, Costes SV, Cucinotta FA. Stochastic properties of radiation-induced
938 DSB: DSB distributions in large scale chromatin loops, the HPRT gene and within the visible
939 volumes of DNA repair foci. Int J Radiat Biol. 2008;84(11):916-29. Epub 2008/11/19.
940 54. Tommasino F, Friedrich T, Jakob B, Meyer B, Durante M, Scholz M. Induction and
941 Processing of the Radiation-Induced Gamma-H2AX Signal and Its Link to the Underlying
942 Pattern of DSB: A Combined Experimental and Modelling Study. PLoS One.
943 2015;10(6):e0129416. Epub 2015/06/13.
944 55. Lorat Y, Schanz S, Schuler N, Wennemuth G, Rübe C, Rübe CE. Beyond repair foci:
945 DNA double-strand break repair in euchromatic and heterochromatic compartments analyzed by
946 transmission electron microscopy. PLoS One. 2012;7(5):e38165. Epub 2012/06/06.
947 56. Aydin OZ, Vermeulen W, Lans H. ISWI chromatin remodeling complexes in the DNA
948 damage response. Cell Cycle. 2014;13(19):3016-25. Epub 2014/12/09.
949 57. Broustas CG, Lieberman HB. DNA damage response genes and the development of
950 cancer metastasis. Radiat Res. 2014;181(2):111-30. Epub 2014/01/09.
951 58. Kouzarides T. Chromatin modifications and their function. Cell. 2007;128(4):693-705.
952 Epub 2007/02/27.
953 59. Jakob B, Splinter J, Taucher-Scholz G. Positional stability of damaged chromatin
954 domains along radiation tracks in mammalian cells. Radiat Res. 2009;171(4):405-18.
955 60. Jakob B, Scholz M, Taucher-Scholz G. Biological imaging of heavy charged-particle
956 tracks. Radiat Res. 2003;159(5):676-84. Epub 2003/04/25.
957 61. Du G, Drexler GA, Friedland W, Greubel C, Hable V, Krucken R, et al. Spatial dynamics
958 of DNA damage response protein foci along the ion trajectory of high-LET particles. Radiat Res.
959 2011;176(6):706-15.
960

961

962 ## Supporting information

963 **Fig. 1: Representation of the microbeam irradiation (*14*).** [A] and [B] An endothelial cell
964 monolayer is positioned perpendicularly to the beam (red arrows) so that each charged particle
965 traversing the cell nucleus (average thickness 2.4 μm) deposits its energy along the particle track.
966 The yellow dots symbolize clusters of energy deposition in the cell nucleus. [C] In the
967 observation with microscopy methodology for *in situ* 53BP1 or γ-H2AX foci detection, foci
968 within a track overlap. For comparison of the simulations with the observations, multiple z-planes
969 were collapsed as 2D projection to obtain a number of simulated foci.

970

971 **Fig. 2: Characterization of 53BP1 and γ-H2AX foci background.** Distribution of the number
972 of 53BP1 or γ-H2AX foci per nucleus in G_0/G_1 phase of the cell cycle for the five and seven
973 replicate experiments related, respectively, to control (Panel A) and sham-treated dishes (Panel
974 B). For each replicate experiment (noted C1, C2 …and S1, S2 ...), the number of cell nuclei is
975 indicated between parentheses. To take into account the inter-dish variability and to increase the
976 statistical power of the analysis, control and sham data were individually pooled with the total
977 number of cell nuclei indicated between parentheses (Panel C). The mean number of foci per
978 nucleus (m_{pool}) represents the mean of the distribution of given pooled data and is associated with
979 the standard deviation (SD) computed as the square root of the variance of the given pooled
980 distribution.

981

982 **Fig. 3: Definition of square pattern of irradiation and revelation of irradiation pattern by**
983 **53BP1 and γ-H2AX foci formation.** [A] Each cell nucleus was targeted by five particles

according to a cross pattern with the middle one positioned at the barycenter of the cell nucleus. The sides of the square measure 4 μm. [B] The cultures were fixed for analysis at 10 min after exposure to 20 MeV α particles. [B-1]: stained with DAPI, [B-2]: 53BP1 immunodetection (red), [B-3]: γ-H2AX immunodetection (green), [B-4]: images in panels A-C are superimposed. (scale bar = 6 μm).

Fig. 4: Distribution of number of 53BP1 and γ-H2AX foci per nucleus following exposure of each cell nucleus of each replicate experiment by five distinct particles placed at different positions. For each irradiation condition (type and quality of ionizing radiation listed in Table 1), and for each replicate experiment (noted I1, I2 …), the number of cell nuclei is indicated between parentheses. The mean number of 53BP1 and γ-H2AX foci per nucleus, $m_r \pm SE$, expressed as the mean of the means and as the SE between the means obtained between replicate experiments are indicated on each graph as well as the standard error of the mean (SEM), computed as the SE divided by the square root of the number of replicates. While five ionizing particles have theoretically reached each cell nucleus, the distribution can spread from zero up to ten 53BP1 or γ-H2AX foci per nucleus and differs as a function of the respective radiation quality used.

Fig. 5: Estimated relative frequencies of at least one 53BP1 or γ-H2AX focus formation following a particle traversal as a function of the LET of the radiation and impact of different corrections due to experimental conditions. Relative frequencies of observed foci formation per particle track traversing 2.4 μm thickness of endothelial cell nucleus based on raw data (purple symbols) as a function of the LET of protons (circles) and α particles (diamonds) for each replicate experiment (open symbols) as well as the mean of all replications for each irradiation condition (closed symbols) are plotted for, respectively, 53BP1 [A] and γ-H2AX [B].

[C] and [D] represent, respectively for 53BP1 and γ-H2AX, the previous curve (purple symbols), sham background subtracted curve (green symbols), combined with the corrections for the number of particles hitting cell nuclei (orange symbols) and for foci related to different particle tracks that are too close to be distinguished (red symbols). The LET of primary ionizing particles was ~19 keV·µm^{-1} (1.6 MeV protons), ~36 keV·µm^{-1} (17.8 MeV α particles), ~85 keV·µm^{-1} (5.5 MeV α particles) (LET), 1.86 MeV α particles (LET ~170 keV·µm^{-1}). The red curve represents the best estimates of relative frequencies of at least one radiation-induced 53BP1 and γ-H2AX focus formation as a function of the LET of the ionizing particle traversing 2.4 µm thickness of endothelial cell nucleus. (* $P<0.05$; ** $P<0.01$, *** $P<0.001$)

Fig. 6: Example of the relation between the relative frequencies of foci per particle traversal "observable in microscopy" and the assumed probabilities of conversion from a particle track into an artificial focus. From simulated coordinates of each particle traversal in a given nucleus, a Bernoulli schema with success probability of conversion of particle tracks into foci from 0 to 1 by steps of 0.05 was applied. For a given probability of conversion, a set of artificial foci is generated, and only the pairs of them located less than 2 µm away are combined (reflecting the observable foci, as they are not distinguishable in microscopy). Thus, we obtain a relation between relative frequencies of supposedly observable foci (after association of foci in too close proximity) and the underlying theoretical probabilities of particles interacting at least once with DNA along the particle track in nucleus thickness. As this relation depends on the initial irradiation characteristics (beam size and cell morphology), the relation was established for each replicate experiment of each irradiation condition.

Fig. 7: Comparison of relative frequencies of at least one focus formation per particle track converted from 2.4 to 2 µm-thick endothelial cell nucleus and results based on Monte Carlo simulation with cell nucleus thickness of 2 µm as a function of LET of incident projectile. For the sake of comparison to the simulations, the biological relative frequencies of at least one focus formation following a particle traversal were, beforehand, converted to the probability per 2 µm path length based on Markov property (memoryless property) with quantity of DNA traversed and constant LET of the particle. In simulated results, we considered that each simulated DNA DSB was induced by a minimum number of clustered DNA SBs varying here from to two to four and that every simulated DNA DSB along the track is converted into a detectable focus (blue curves).

Supplementary Fig. 1: Visualization of variation in cells' morphology and fixed irradiation pattern. [A] Simulation of each cell nucleus of the cell population, as an ellipse considering their specific major and minor axes and their orientation; [B] Each cell nucleus was exposed to the same theoretical pattern of five particles placed at the extremity of a 4 µm side square with one in the middle, positioned at the barycenter of each cell nucleus; [C] The coordinates of each particle hit of the irradiation pattern with respect to the nominal position were sampled from a Gaussian distribution along the x- ($\mu = 0$, $\sigma 1 = d1/2.355$) and y- ($\mu = 0$, $\sigma 2 = d2/2.355$) axes.

Supplementary Fig. 2: Examples of graphic outputs concerning the reconstruction of hit patterns in different cell nuclei. [A] Real nuclei of cell population from irradiated dish; [B] Simulation mimicking the respective cell nucleus as an elliptic shape; [C] Simulated positions of particle hits indicated by red stars and estimated number of particle hits in the cell nuclei that may vary slightly from one nucleus to another depending on irradiation characteristics and cell nuclei geometry. Although each cell nucleus theoretically should have received 5 particles according to

1055 the cross pattern, the number of traversing particles may vary slightly from one nucleus to
1056 another depending on the irradiation characteristics and cell nuclei geometry.
1057 **Supplementary Fig. 3: Relative frequency distribution of the equivalent ellipse [A] major**
1058 **and [B] minor axis, and [C] area of the totality of cell nuclei analyzed in this study.** m and
1059 SD represent, respectively, the mean of the distribution and the standard deviation (SD)
1060 computed as the square root of the variance of the distribution for each parameter analyzed.
1061 **Supplementary Fig. 4: Optimization of the irradiation pattern size.** Probability of getting two
1062 particle hits at a distance of less than 2 µm from one another in a given nucleus (red curves) and
1063 percentage of cell nuclei receiving less than five particle hits (blue curves) were calculated from
1064 simulation and plotted as a function of irradiation pattern size taking into account the real size of
1065 every cell nuclei analyzed for each of the 14 dishes used in this study.
1066 **Supplementary Fig. 5: Influence of time post-irradiation (10 or 30 minutes) on distribution**
1067 **of number of 53BP1 and γ-H2AX foci per nucleus following exposure to 1.6 MeV protons**
1068 **(LET in the nucleus ~19 keV·µm-1) or 5.5 MeV α particles (LET in the nucleus**
1069 **~85 keV·µm-1).** Panel A: Distribution of number of 53BP1 and γ-H2AX foci per nucleus
1070 evaluated for each of the five and six replicate experiments (noted I1, I2, ...) 10 min and 30 min,
1071 respectively, after exposure to 1.6 MeV protons and on three replicate experiments both 10 min
1072 and 30 min after exposure to 5.5 MeV α particles. For each replicate experiment, the number of
1073 cell nuclei is indicated between parentheses. Panel B: Distribution of number of 53BP1 and γ-
1074 H2AX foci per nucleus evaluated as pooled data according to time point. Total number of cells
1075 counted is indicated between parentheses.
1076 **Supplementary Fig. 6: 3D representation of cell nucleus in the simulations through three**
1077 **levels of zoom (*38*).** The cell nucleus phantom is represented by a cylinder with elliptical base of
1078 major semi-axis a = 9.5 µm, minor semi-axis b = 5.5 µm, and 2 µm height. The whole genome of

a eukaryotic cell (~6 Gbp) is distributed in spherical regions representing chromatin domains containing ~1 Mbp. These are placed homogeneously within the cell nucleus phantom in order to simulate cells in the G0/G1 phase of the cell cycle. Each of these chromatin domains was filled with voxels containing a geometrical representation of the chromatin fiber of helicoidal shape.

Table 1: Physical characteristics of the beam for the different projectiles and energies used for biological experiments

Selected Beam Energy	Scintillator Thickness (µm)	Biofoil Thickness (µm)	**Estimated energy in the center of cell nucleus (MeV)**	Estimated average LET values in the center of cell nucleus ($keV \cdot \mu m^{-1}$)	Beam size FWHM [a] d_1 x d_2 (µm x µm)	Detection thresholds and noise events in the particle counter (n_0/n_2) [b]
Protons 3 MeV	40	25	**1.6 ± 0.2**	19 ± 2	4.8 × 4.8	1% / 1% [c]
Alpha 20 MeV	10	25	**17.8 ± 0.2**	36 ± 1	4.2 × 3.9	1% / 1% [c]
Alpha 10 MeV	10	25	**5.5 ± 0.4**	85 ± 4	4.5 × 3.5	1% / 1% [c]
Alpha 8 MeV	10	25	**1.9 ± 0.6**	170 ± 40	4.5 × 3.5	0.1% / 1% [d]

[a] Full Width at Half Maximum. Values were measured just before irradiation for each microbeam setup with the same dish full of medium as for cell irradiation.

[b] n_0 represents the percentage of particles NOT emitted but considered as delivered due to detection of noise events, being zero particle delivered instead of one at each position of the pattern.

n_2 represents the percentage of particles emitted but NOT detected leading to delivery of a second particle, being two particles delivered instead of one at each position of the pattern.

[c] Estimation of scintillator signal

[d] Evaluation of scintillator signal

Table 2: Number of cells analyzed, theoretical number of emitted particles, mean assesses number of particles hits, percentage of ionizing particle hitting a cell nucleus and percentage of cell nuclei receiving exactly 5 particles hits for each dish as a function of type and quality of ionizing radiation

	Samples number	Number of cells *(n)*	Theoretical number of emitted particles *(n X 5 particles hits)*	Mean assessed number of particle hits in nuclei	Percentage of ionizing particle hitting a cell nucleus	Percentage of cell nuclei receiving exactly 5 particles hits[1]
1.6 MeV protons (19 keV·µm^{-1})	1	709	3545	3478.6	98.1	90.4
	2	997	4985	4907.4	98.4	90.6
	3	751	3755	3688.3	98.2	90.6
	4	793	3965	3879.9	97.9	87.8
	5	888	4440	4376.6	98.6	91.6
	6	868	4340	4265.7	98.3	91.2
	Pool	***5006***	***25030***	***24596.5***	***98.3***	***90.4***
17.8 MeV α particles (36 keV·µm^{-1})	1	3374	16870	16275.2	96.5	89.0
	2	3703	18515	18338.9	99.0	93.8
	3	4156	20780	20565.9	99.0	93.5
	Pool	***11233***	***56165***	***55180***	***98.2***	***92.2***
5.5 MeV α particles (85 keV·µm^{-1})	1	2864	14320	13854.0	96.7	83.7
	2	2794	13970	13816.6	98.9	93.1
	3	3058	15290	15137.4	99.0	93.6
	Pool	***8716***	***43580***	***42808***	***98.2***	***90.2***
1.86 MeV α particles (170 keV·µm^{-1})	1	2697	13485	13407.6	99.4	95.3
	2	3071	15355	15290.7	99.6	95.8
	Pool	***5768***	***28840***	***28698.3***	***99.5***	***95.6***

[1] Most of the remaining cell nuclei were hit by 4 or 6 particles.

[A] Passage of ionizing particle through the nucleus

[B] Energy deposition and radiation-induced foci formation along the particle track

[C] 2D projection permits observing radiation-induced foci with microscopy methodology used in biological experiments

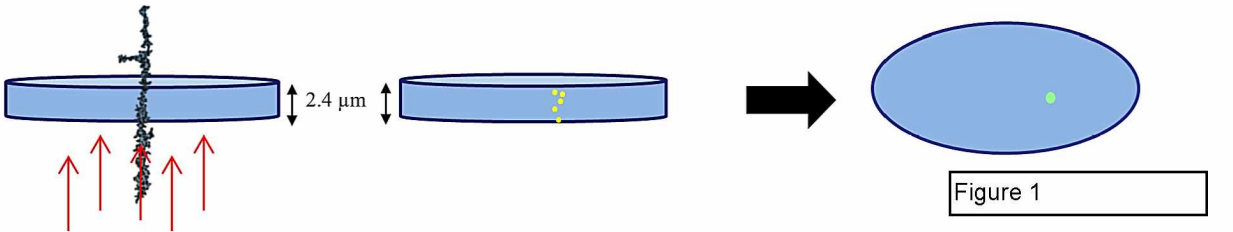

Figure 1

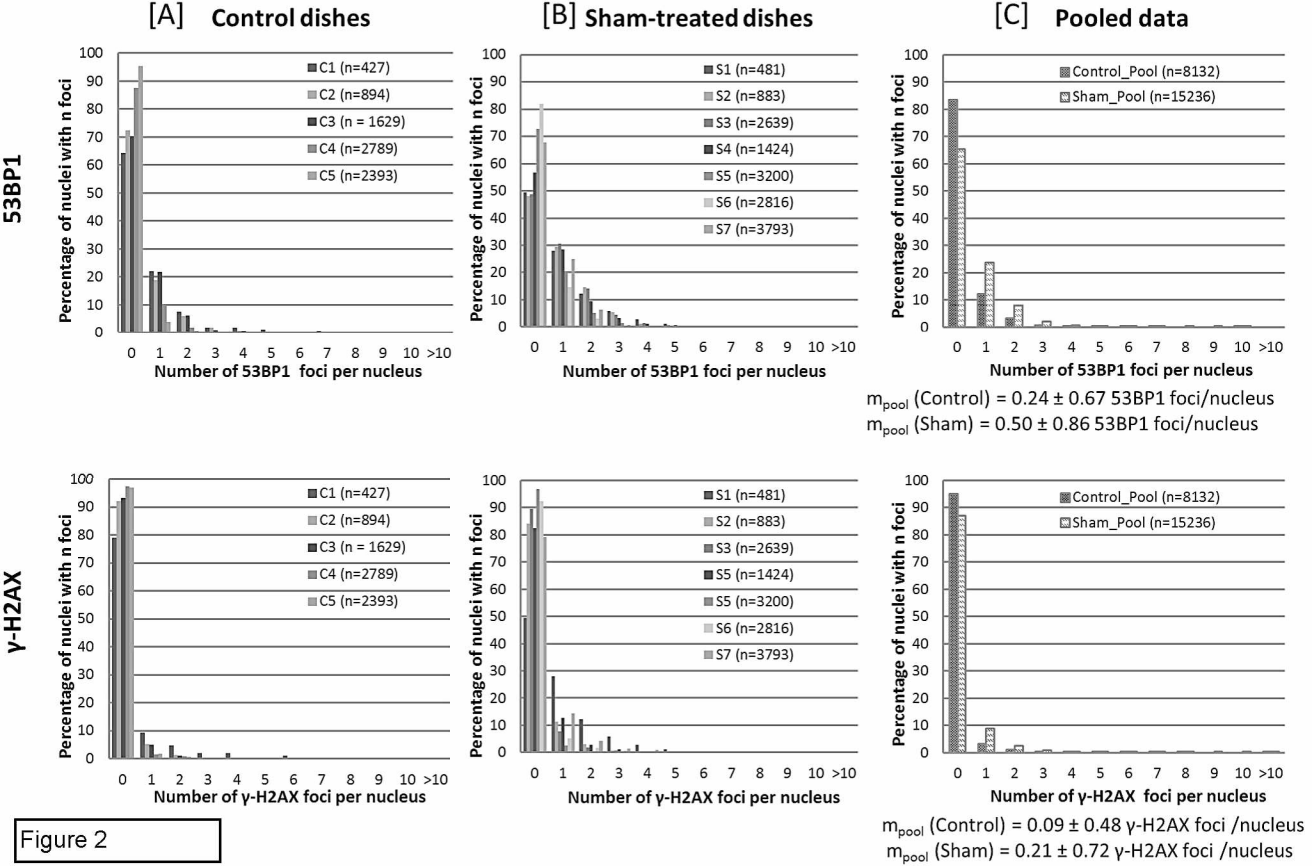
[A] Control dishes
[B] Sham-treated dishes
[C] Pooled data
53BP1
γ-H2AX
Percentage of nuclei with n foci
Number of 53BP1 foci per nucleus
Number of γ-H2AX foci per nucleus
C1 (n=427)
C2 (n=894)
C3 (n = 1629)
C4 (n=2789)
C5 (n=2393)
S1 (n=481)
S2 (n=883)
S3 (n=2639)
S4 (n=1424)
S5 (n=3200)
S6 (n=2816)
S7 (n=3793)
Control_Pool (n=8132)
Sham_Pool (n=15236)
m_pool (Control) = 0.24 ± 0.67 53BP1 foci/nucleus
m_pool (Sham) = 0.50 ± 0.86 53BP1 foci/nucleus
m_pool (Control) = 0.09 ± 0.48 γ-H2AX foci /nucleus
m_pool (Sham) = 0.21 ± 0.72 γ-H2AX foci /nucleus

Figure 2

[A] Definition of the square pattern of irradiation

Figure 3

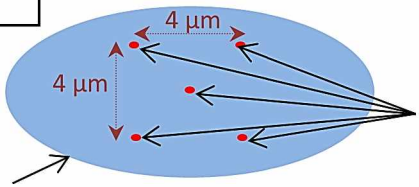

[B] Revelation of the irradiation pattern by 53BP1 and γ-H2AX foci formation

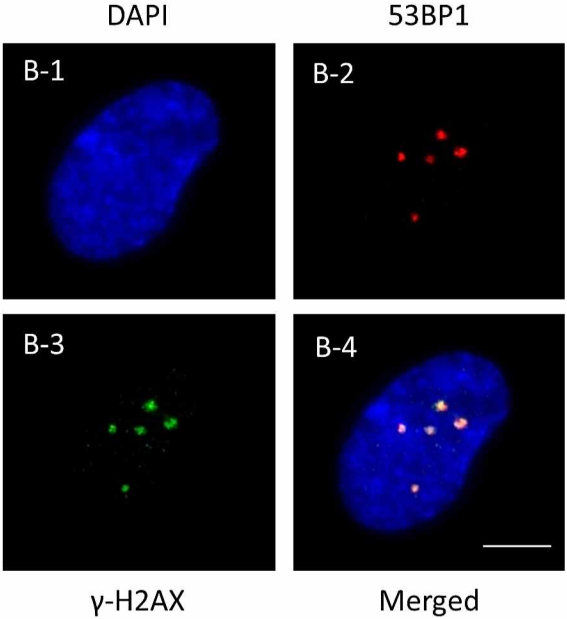

Figure 4

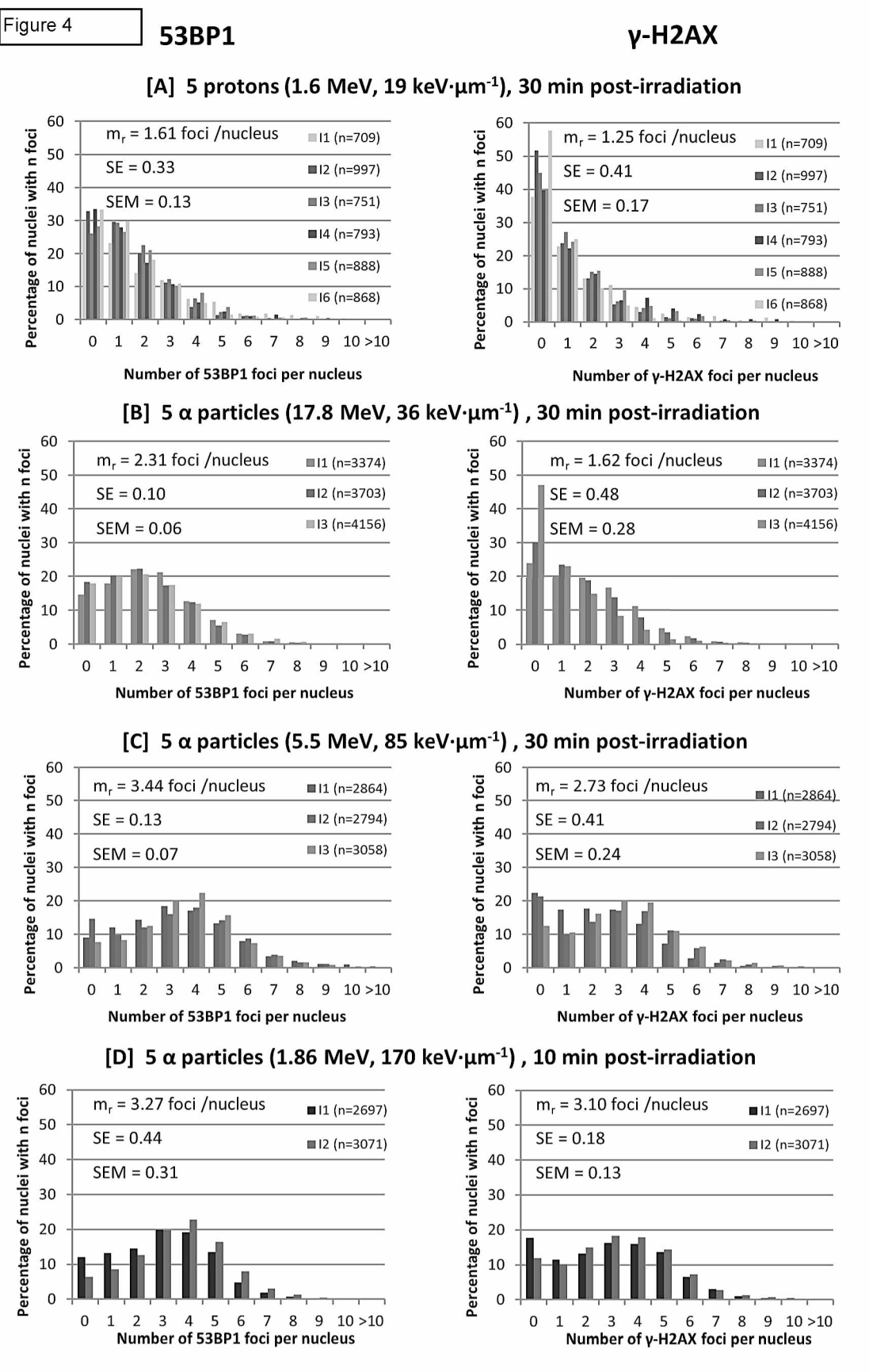
53BP1
γ-H2AX
[A] 5 protons (1.6 MeV, 19 keV·µm-1), 30 min post-irradiation
mr = 1.61 foci /nucleus
SE = 0.33
SEM = 0.13
I1 (n=709)
I2 (n=997)
I3 (n=751)
I4 (n=793)
I5 (n=888)
I6 (n=868)
Percentage of nuclei with n foci
Number of 53BP1 foci per nucleus
mr = 1.25 foci /nucleus
SE = 0.41
SEM = 0.17
Number of γ-H2AX foci per nucleus
[B] 5 α particles (17.8 MeV, 36 keV·µm-1) , 30 min post-irradiation
mr = 2.31 foci /nucleus
SE = 0.10
SEM = 0.06
I1 (n=3374)
I2 (n=3703)
I3 (n=4156)
mr = 1.62 foci /nucleus
SE = 0.48
SEM = 0.28
[C] 5 α particles (5.5 MeV, 85 keV·µm-1) , 30 min post-irradiation
mr = 3.44 foci /nucleus
SE = 0.13
SEM = 0.07
mr = 2.73 foci /nucleus
SE = 0.41
SEM = 0.24
[D] 5 α particles (1.86 MeV, 170 keV·µm-1) , 10 min post-irradiation
mr = 3.27 foci /nucleus
SE = 0.44
SEM = 0.31
I1 (n=2697)
I2 (n=3071)
mr = 3.10 foci /nucleus
SE = 0.18
SEM = 0.13
0 1 2 3 4 5 6 7 8 9 10 >10

[A] Figure 5

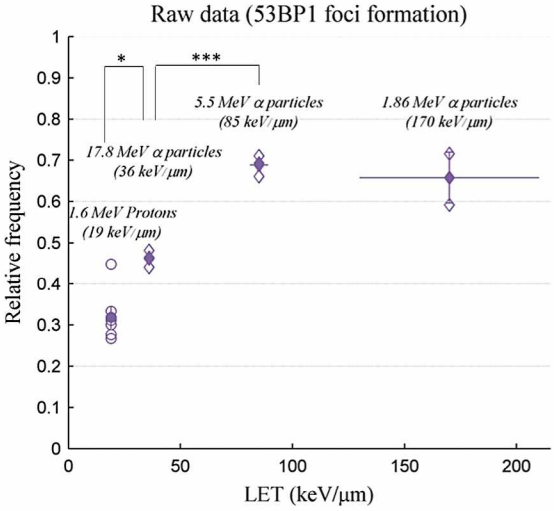

[B]

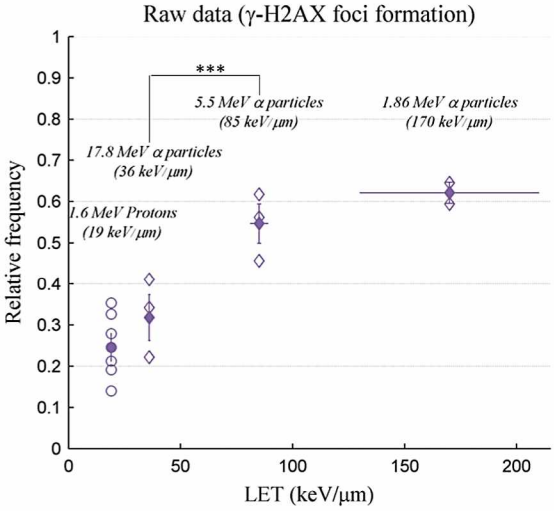

[C]

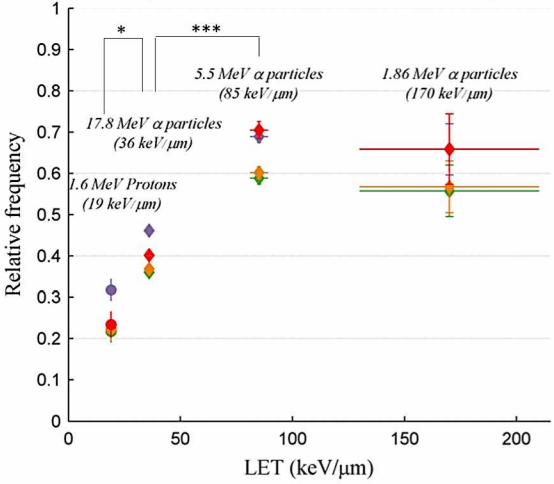

[D]

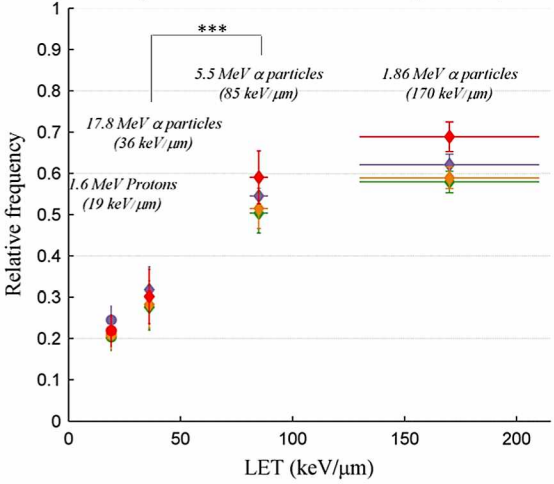

Figure 6

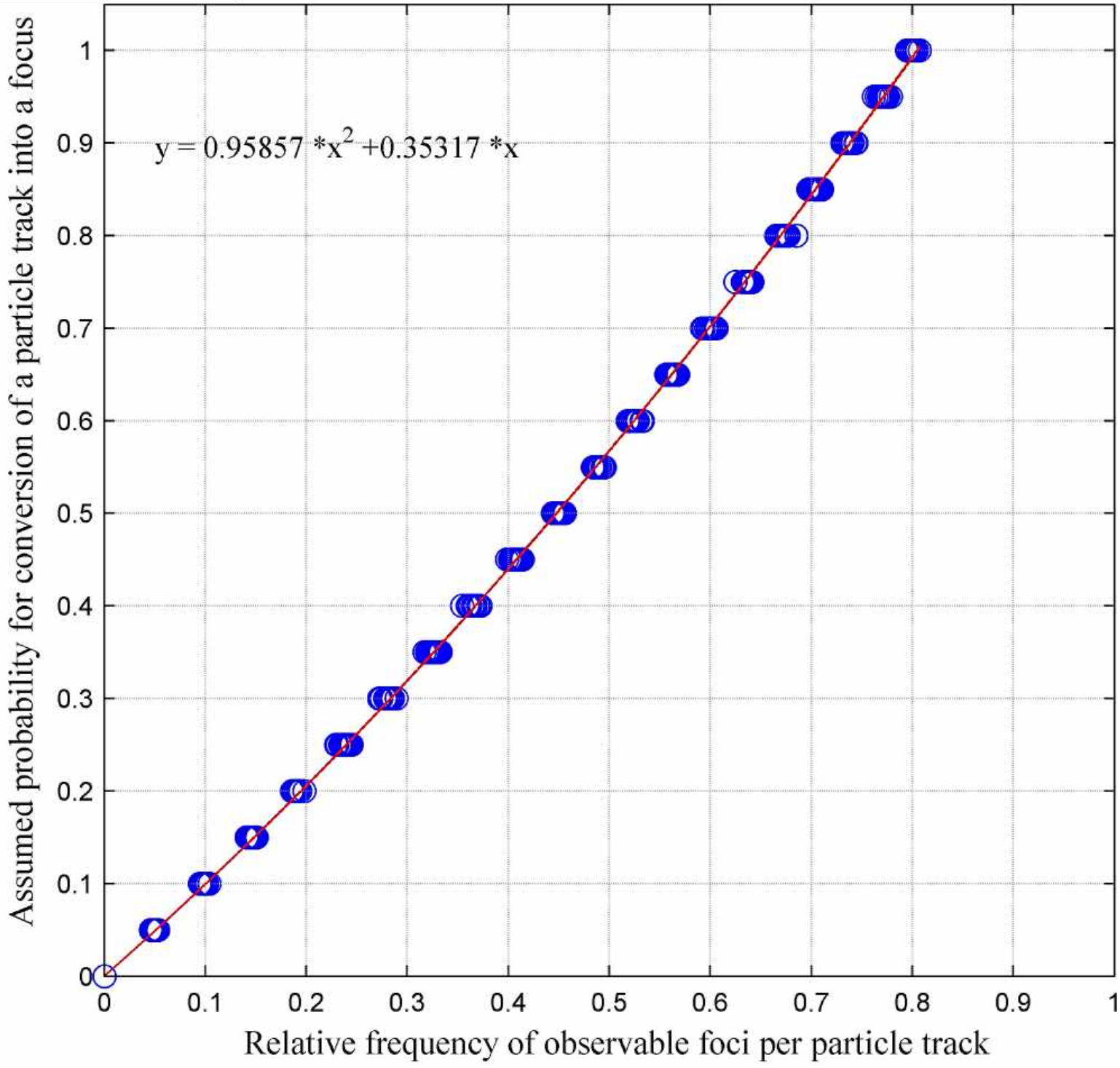
y = 0.95857 *x^2 +0.35317 *x
Assumed probability for conversion of a particle track into a focus
Relative frequency of observable foci per particle track
0
0.1
0.2
0.3
0.4
0.5
0.6
0.7
0.8
0.9
1

Figure 7

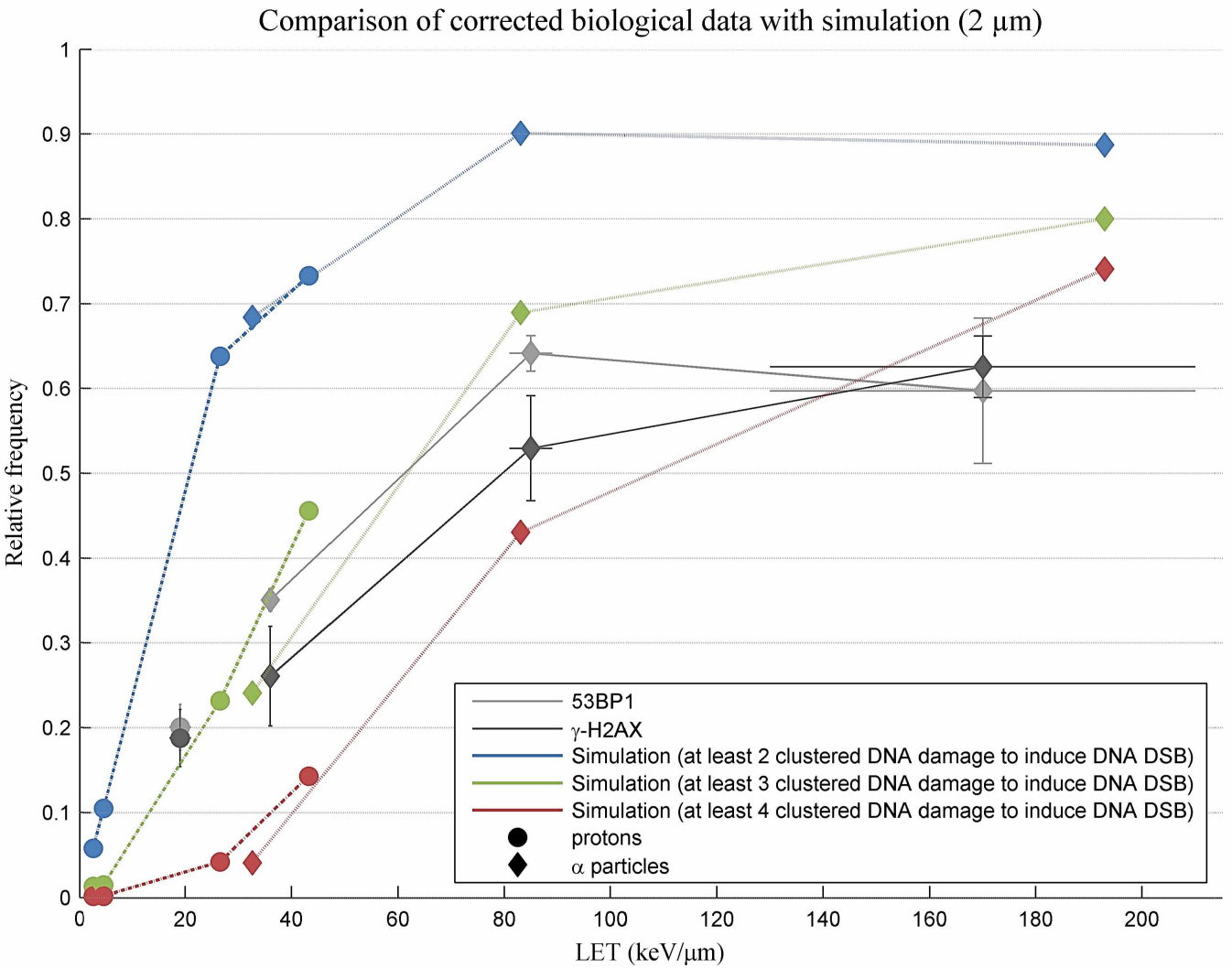
Comparison of corrected biological data with simulation (2 µm)
Relative frequency
LET (keV/µm)
0
0.1
0.2
0.3
0.4
0.5
0.6
0.7
0.8
0.9
1
0
20
40
60
80
100
120
140
160
180
200
53BP1
γ-H2AX
Simulation (at least 2 clustered DNA damage to induce DNA DSB)
Simulation (at least 3 clustered DNA damage to induce DNA DSB)
Simulation (at least 4 clustered DNA damage to induce DNA DSB)
protons
α particles

Supplementary Table 1: Mean number ± SEM of simulated DNA DSB along the track in a 2 µm-thick simulated nucleus as a function of radiation type (0.5, 1, 10, 20 MeV protons, and 1.66, 5.27, 17.39 MeV α particles) and of minimum number of clustered DNA damages taken into account to produce a DNA DSB. The standard error of the mean (SEM) is computed as the SE divided by the square root of the number of incident projectiles simulated.

	LET at the cell center position *(keV·µm^{-1})*	Mean number of predicted DNA DSB along the track in a 2 µm-thick simulated nucleus according to the minimum number of clustered DNA damages inducing one DNA DSB		
		2	**3**	**4**
20 MeV protons	3	0.1 ± 0.0	0.0 ± 0.0	0.0 ± 0.0
10 MeV protons	5	0.1 ± 0.0	0.0 ± 0.0	0.0 ± 0.0
1 MeV protons	26	1.4 ± 0.0	0.3 ± 0.0	0.0 ± 0.0
17.39 MeV α particles	32	1.5 ± 0.0	0.3 ± 0.0	0.0 ± 0.0
0.5 MeV protons	43	2.8 ± 0.1	0.8 ± 0.0	0.2 ± 0.0
5.27 MeV α particles	83	6.6 ± 0.2	2.3 ± 0.1	0.7 ± 0.0
1.66 MeV α particles	193	18.3 ± 0.5	11.0 ± 0.3	5.8 ± 0.2

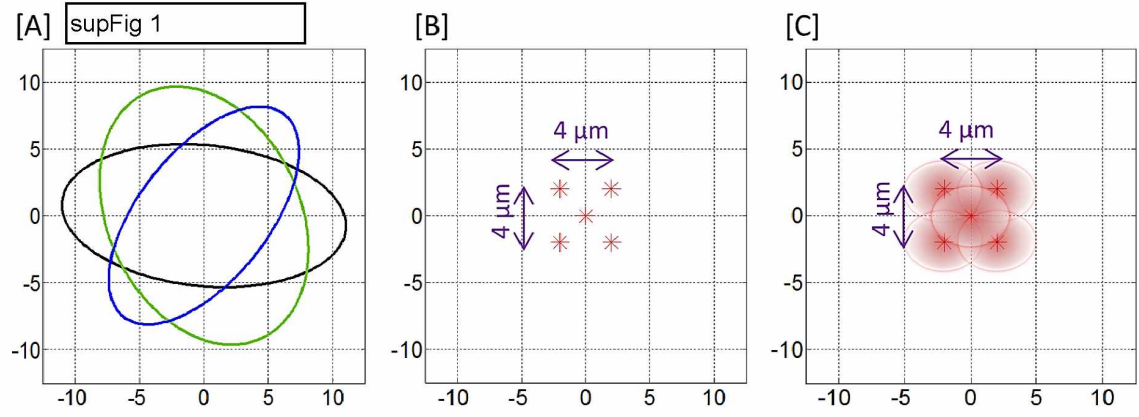
[A]
supFig 1
[B]
4 µm
4 µm
[C]
4 µm
4 µm
10
5
0
-5
-10
-10
-5
0
5
10

SupFig 2

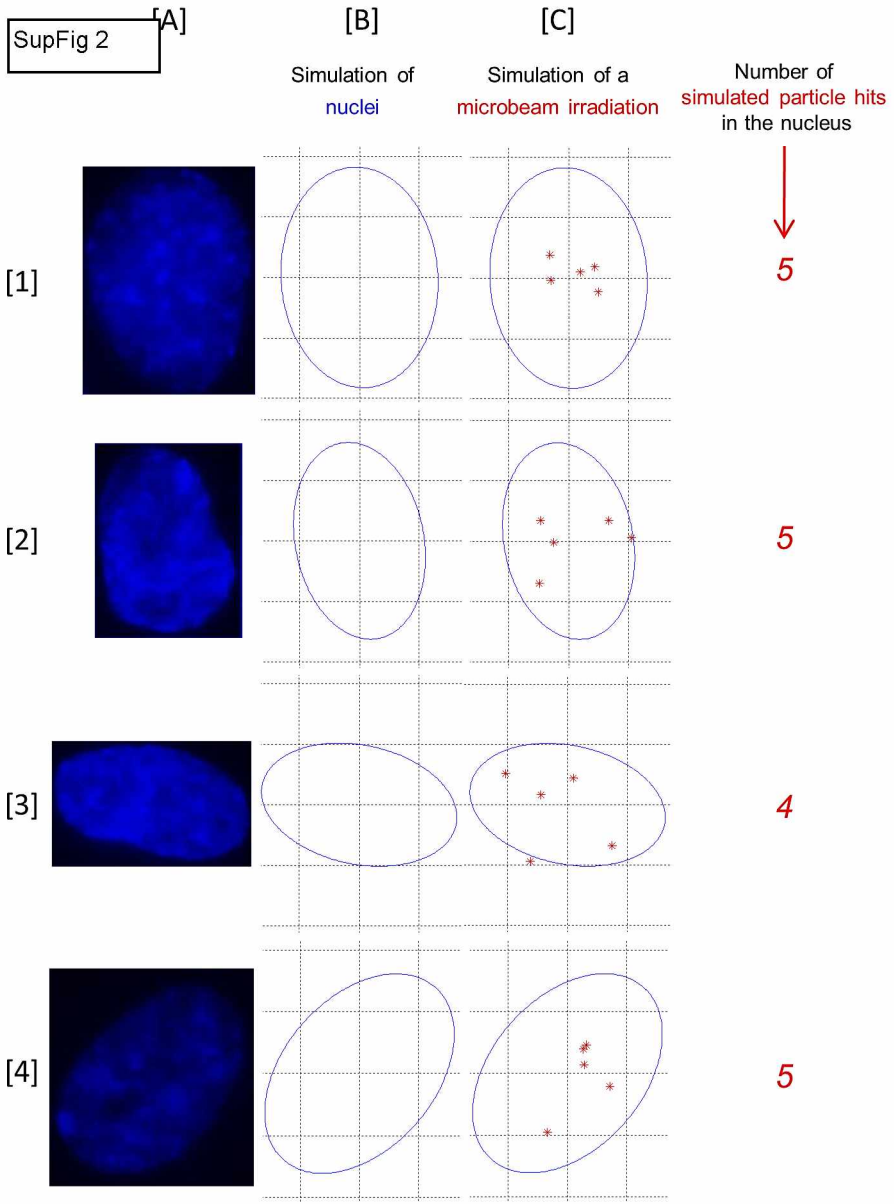
[A]
[B]
[C]
Simulation of nuclei
Simulation of a microbeam irradiation
Number of simulated particle hits in the nucleus
[1]
5
[2]
5
[3]
4
[4]
5

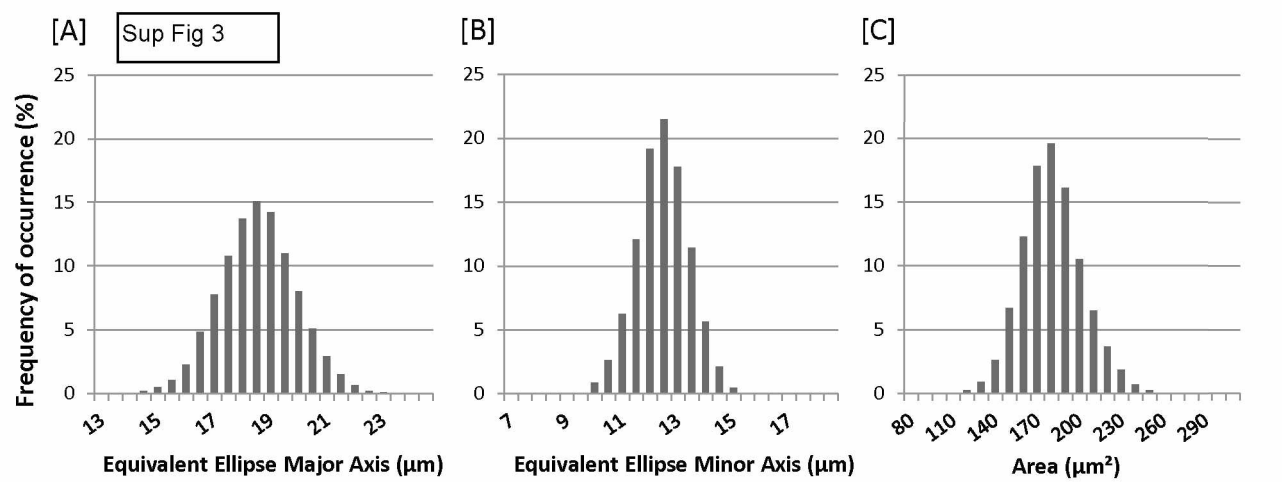

m = 18.3 µm
SD = 1.4 µm
min = 13.7 µm
max = 23.8 µm

m = 12.2 µm
SD = 0.9 µm
min = 9.2 µm
max = 16.0 µm

m = 175.9 µm²
SD = 21.5 µm²
min = 103.2 µm²
max = 277.6 µm²

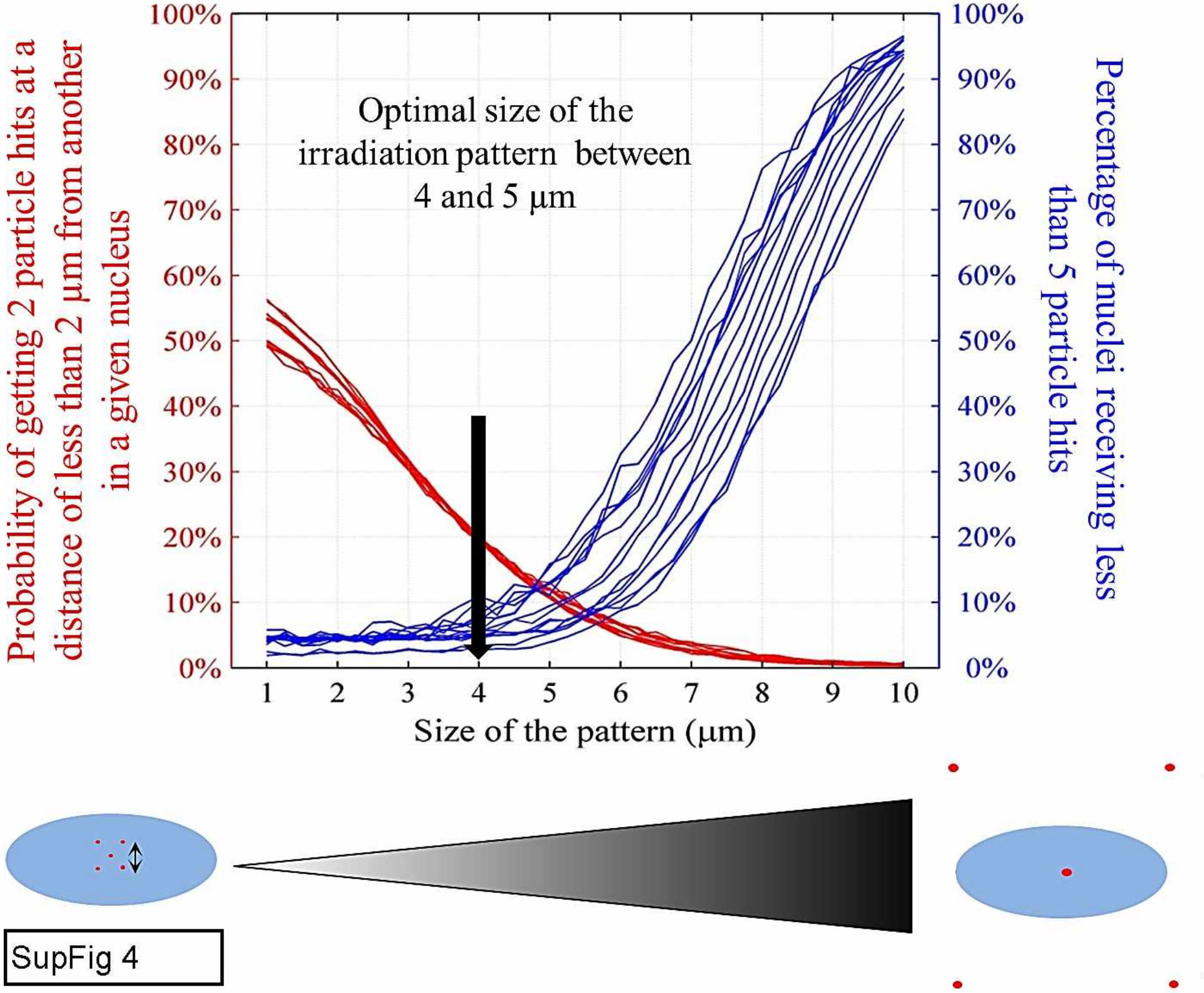
Probability of getting 2 particle hits at a distance of less than 2 µm from another in a given nucleus
Percentage of nuclei receiving less than 5 particle hits
Optimal size of the irradiation pattern between 4 and 5 µm
100%
90%
80%
70%
60%
50%
40%
30%
20%
10%
0%
1
2
3
4
5
6
7
8
9
10
Size of the pattern (µm)

SupFig 4

SupFig 5

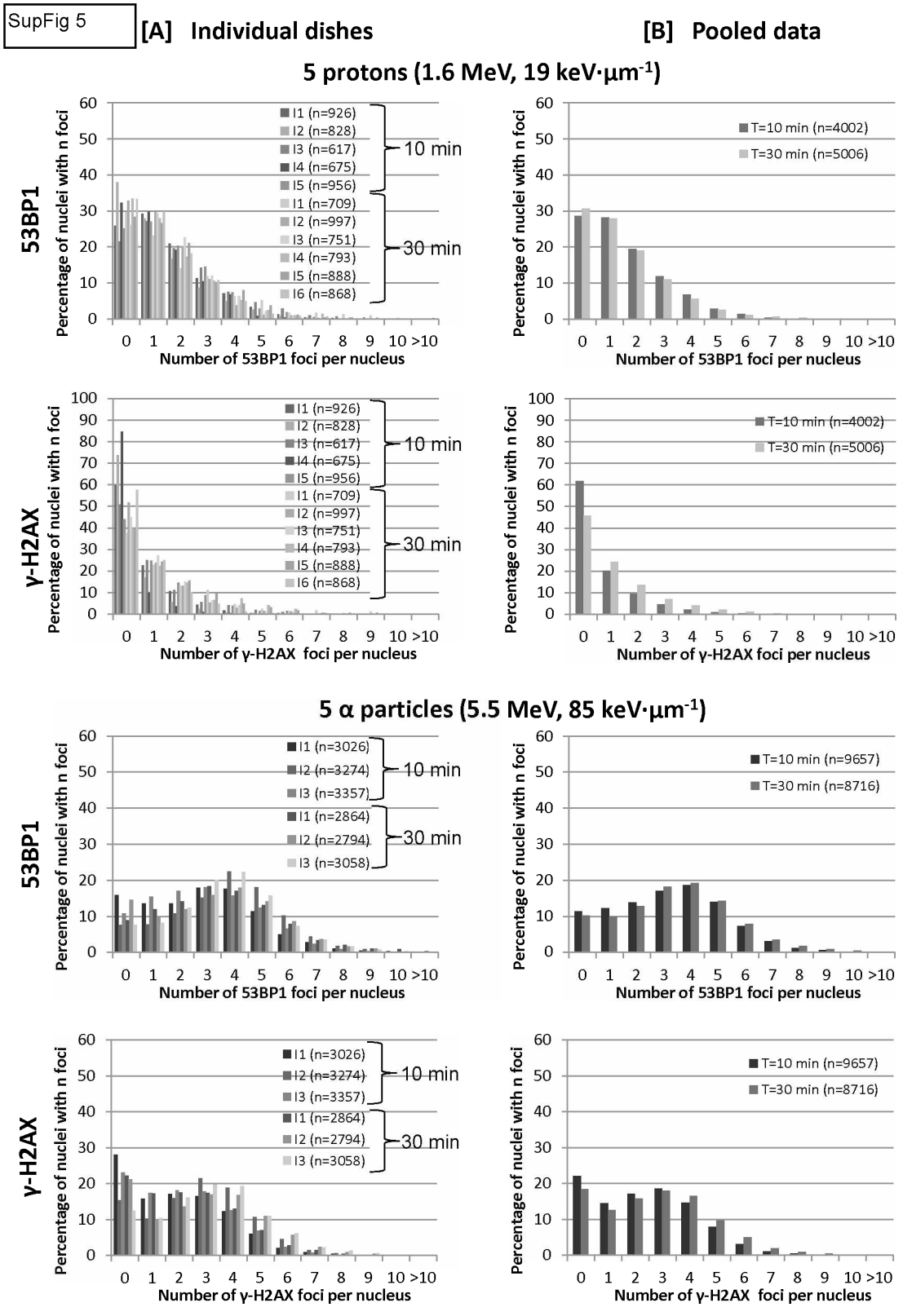
[A] Individual dishes
[B] Pooled data
5 protons (1.6 MeV, 19 keV·µm-1)
53BP1
γ-H2AX
Percentage of nuclei with n foci
Number of 53BP1 foci per nucleus
Number of γ-H2AX foci per nucleus
I1 (n=926)
I2 (n=828)
I3 (n=617)
I4 (n=675)
I5 (n=956)
I1 (n=709)
I2 (n=997)
I3 (n=751)
I4 (n=793)
I5 (n=888)
I6 (n=868)
10 min
30 min
T=10 min (n=4002)
T=30 min (n=5006)
5 α particles (5.5 MeV, 85 keV·µm-1)
I1 (n=3026)
I2 (n=3274)
I3 (n=3357)
I1 (n=2864)
I2 (n=2794)
I3 (n=3058)
T=10 min (n=9657)
T=30 min (n=8716)

SupFig 6